

Virtual and Physical Prototyping

ISSN: (Print) (Online) Journal homepage: https://www.tandfonline.com/loi/nvpp20

Topology optimisation of self-supporting structures based on the multi-directional additive manufacturing technique

Jun Ye, Qichen Guo, Hongjia Lu, Pinelopi Kyvelou, Yang Zhao, Leroy Gardner & Yi Min Xie

To cite this article: Jun Ye, Qichen Guo, Hongjia Lu, Pinelopi Kyvelou, Yang Zhao, Leroy Gardner & Yi Min Xie (2023) Topology optimisation of self-supporting structures based on the multi-directional additive manufacturing technique, Virtual and Physical Prototyping, 18:1, e2271458, DOI: 10.1080/17452759.2023.2271458

To link to this article: https://doi.org/10.1080/17452759.2023.2271458

© 2023 The Author(s). Published by Informa UK Limited, trading as Taylor & Francis Group

Published online: 01 Nov 2023.

Submit your article to this journal

View related articles

View Crossmark data

Full Terms & Conditions of access and use can be found at
https://www.tandfonline.com/action/journalInformation?journalCode=nvpp20

VIRTUAL AND PHYSICAL PROTOTYPING
2023, VOL. 18, NO. 1, e2271458 (21 pages)
https://doi.org/10.1080/17452759.2023.2271458

Taylor & Francis
Taylor & Francis Group

OPEN ACCESS Check for updates

Topology optimisation of self-supporting structures based on the multi-directional additive manufacturing technique

Jun Ye[a,b,c], Qichen Guo[a,b], Hongjia Lu[d], Pinelopi Kyvelou[e], Yang Zhao[a], Leroy Gardner[e] and Yi Min Xie[d]

[a]College of Civil Engineering and Architecture, Zhejiang University, Hangzhou, People's Republic of China; [b]Centre for Balance Architecture, Zhejiang University, Hangzhou, People's Republic of China; [c]School of Civil Engineering, University of Leeds, Leeds, UK; [d]Centre for Innovative Structures and Materials, School of Engineering, RMIT University, Melbourne, Australia; [e]Department of Civil and Environmental Engineering, Imperial College London, London, UK

ABSTRACT

Although additive manufacturing (AM) continues to gain widespread adoption, the overhang problem remains a critical issue affecting printing quality. The design of self-supporting structures via topology optimisation approaches has been extensively studied. However, current optimisation research predominantly focuses on 3-axis AM machines, overlooking the more recently developed multi-axis machines. Moreover, the performance sacrifice due to overhang constraints in 3-axis AM can be significant, especially in structures with small volume fractions. To address this, we propose a two-step approach considering overhang constraints for multi-axis AM. This approach begins with a structure optimised using traditional topology optimisation. In the first step, a new optimisation problem determines printing surfaces for the given structure. If the proportion of unprintable elements isn't satisfactory, a second re-optimisation step is carried out to further reduce the unprintable proportion. Several examples demonstrate the effectiveness of the proposed approach. Notably, the significant performance sacrifice associated with the 3-axis AM approach becomes negligible when applying our multi-axis AM-based method.

ARTICLE HISTORY
Received 27 July 2023
Accepted 10 October 2023

KEYWORDS
Topology optimisation; multi-axis additive manufacturing; overhang constraints; self-supporting structures; performance sacrifice

1. Introduction

Topology optimisation aims to identify structures with optimised performance (e.g. maximum stiffness), while satisfying specified conditions and constraints [1–4]. With the focus across all sectors currently being on enhancing sustainability and reducing carbon emissions, the field of topology optimisation is attracting increasing attention, and it has been applied to many different fields (e.g. automobile, biostructural and aerospace [5–7]). However, although topology optimisation can be used to create high-performance structures [8–10], the optimised free-form shapes are often difficult to produce using traditional manufacturing methods. Thus, seeking to materialise the outcomes of structural optimisation, additive manufacturing (AM) techniques have been recently employed [9,11,12]. The combination of topology optimisation and additive manufacturing has therefore become an active research topic in recent years.

Although AM can be used to print complex geometries, current technologies do not guarantee that structures of any arbitrary shape can be printed [13–16]. One foremost reason is the overhang effect. As illustrated in Figure 1, if the overhang angle φ_{ov} of the component exceeds the maximum threshold angle φ_{max}, the deposited part cannot consolidate due to gravity [17]. To address this problem, temporary support structures are used [18,19]. However, support structures consume additional materials and are difficult to remove in certain cases (e.g. in metal AM). For structures with simple geometries, the influence of the overhang effect can be alleviated, or even eliminated, by changing the build direction. However, identifying a build direction that can eliminate the need for support structures in the case of complex build geometries can be challenging.

In order to avoid the overhang effect and, thus, the use of support structures, some studies have adopted topology optimisation to modify the geometrical shape of the components to be printed. Leary et al. [20,21] used a post-processing approach to design efficient supporting structures for optimised solutions. However, since the resulting structures required

CONTACT Hongjia Lu hongjia.lu@rmit.edu.au Centre for Innovative Structures and Materials, School of Engineering, RMIT University, 264 Plenty Rd, Mill Park, Melbourne, VIC 3082, Australia

© 2023 The Author(s). Published by Informa UK Limited, trading as Taylor & Francis Group
This is an Open Access article distributed under the terms of the Creative Commons Attribution-NonCommercial License (http://creativecommons.org/licenses/by-nc/4.0/), which permits unrestricted non-commercial use, distribution, and reproduction in any medium, provided the original work is properly cited. The terms on which this article has been published allow the posting of the Accepted Manuscript in a repository by the author(s) or with their consent.

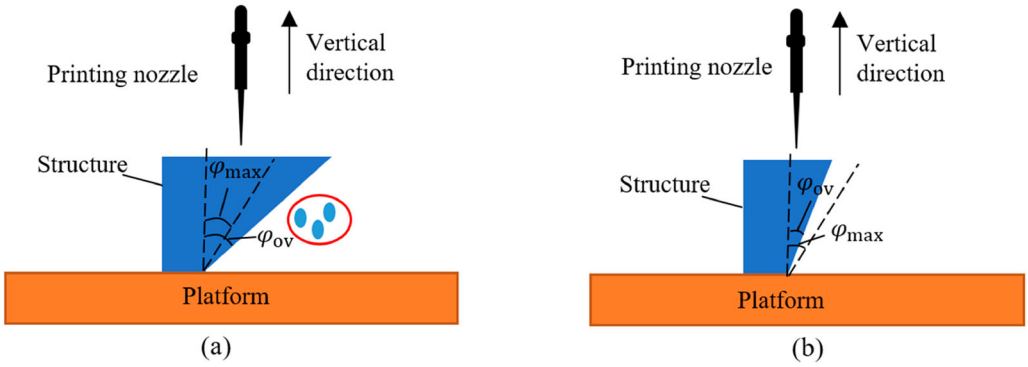


Figure 1. The overhang effect: (a) structure failing to consolidate when the overhang angle φ_{ov} is greater than the overhang threshold φ_{max}; (b) structure successfully consolidating when the overhang angle φ_{ov} is less than φ_{max}.

additional supporting materials, the volume fraction (i.e. the ratio between the structural volume and the design domain volume) constraint of the optimisation formulation was violated. Therefore, subsequent studies included the overhang constraints into the topology optimisation formulation, either by explicitly adding them as constraints or by filtering out the elements violating them. Gaynor et al. [22] considered the overhang constraint through projection methods. Langelaar et al. [23,24] proposed a method that can simultaneously identify and optimise both the main and the supporting structure and determine the corresponding build direction. Pellens et al. [25] addressed the overhang effect by utilising four different elemental filters to eliminate elements that violated the overhang and minimum length scale constraints. Zhang et al. [26] applied overhang constraints by restricting the orientation of the boundaries of the structure using Heaviside projection functions. Garaigordobil et al. [27] used a SUSAN contour detection algorithm to extract the structural boundaries and then applied explicit constraints to the optimisation formulation to avoid the overhang effect. Although the findings of these studies can be used to eliminate the emergence of excessively overhanging parts, the overhang constraints considered were based on 3-axis AM. Consequently, the sacrifice in performance caused by the overhang constraints was usually high, especially in problems with low volume-fraction values [28].

Besides the aforementioned optimisation-related research, other studies have focused on addressing the overhang problem by improving the machine flexibility; hence AM machines with multi-axis configurations have been developed in recent years. Multi-axis machines differ from 3-axis machines by having rotatable platforms that allow for continuous build direction adjustments [29] (Figure 2), enabling the printing of curved surfaces [30,31]. Therefore, some studies [32–34] have focused on reducing the overhang effect by decomposing the structure into

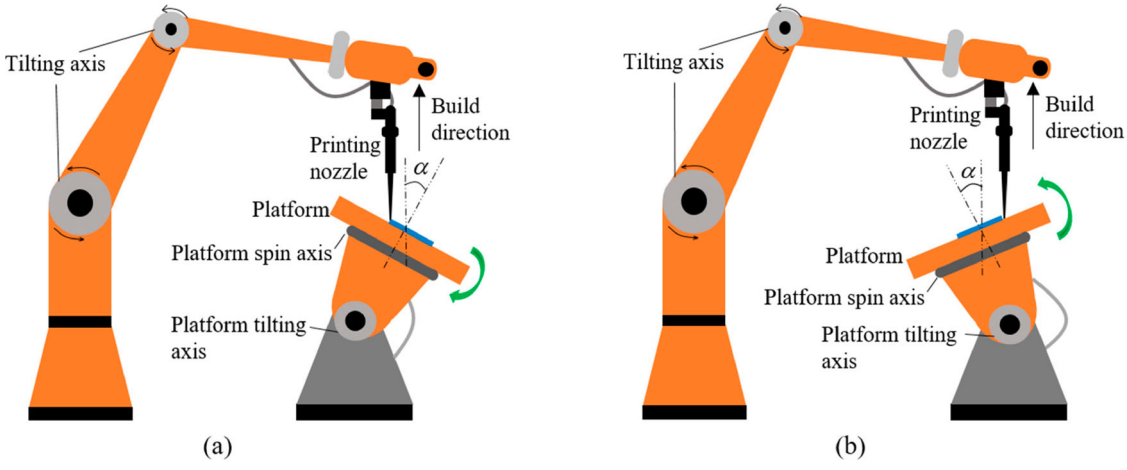


Figure 2. Multi-axis AM machine: (a) the platform rotates clockwise; (b) the platform rotates counterclockwise, where α denotes the platform tilting angle.

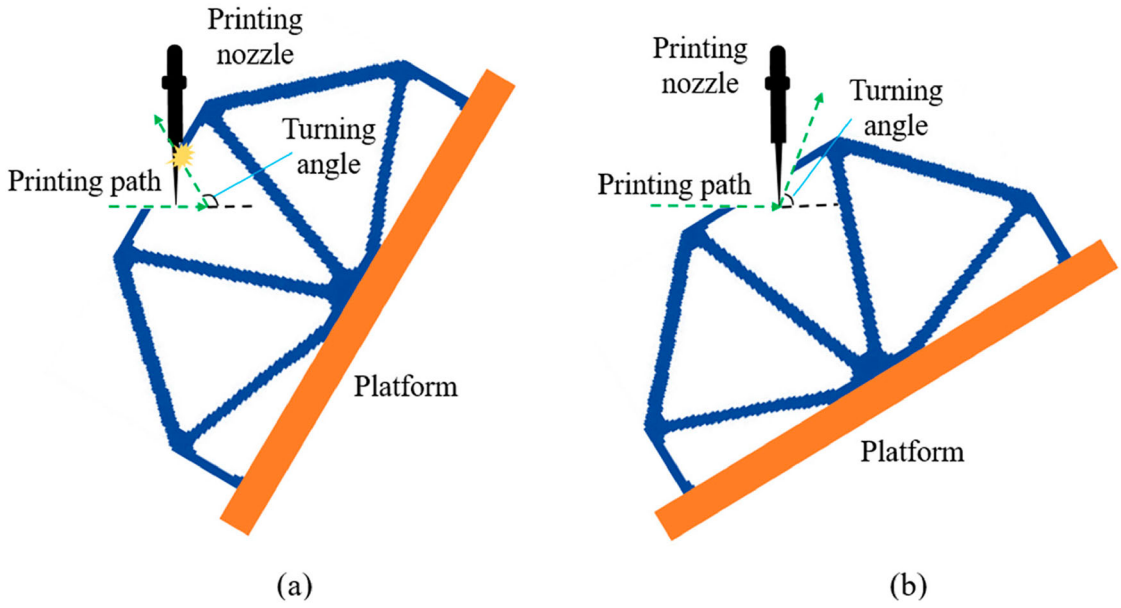


Figure 3. Effect of different printing surfaces: (a) deep concave surface with a large turning angle leads to a collision between the printing nozzle and the printed part; (b) the collision can be avoided by reducing the turning angle of the printing surface.

several parts and applying different local build directions for each part. Further studies customised the curved printing surfaces to reduce the overhang effect [35–37]. However, the utilisation of curved printing surfaces can potentially result in collisions between the printing nozzle and the printed part. To elaborate, in 3-axis AM, the printing surfaces are restricted to be horizontal, eliminating the risk of collision. Furthermore, convex and shallow concave surfaces (i.e. characterised by a low turning angle) maintain a negligible risk of collision as shown in Figure 3(b). However, the risk increases when deep concave printing surfaces (i.e. high turning angle) are employed (Figure 3(a)). To address this problem, Li et al. [38] included collision detection in the tool path planning step, to determine collision-free printing tool paths. However, although the aforementioned studies related to multi-axis AM can significantly reduce the required support materials, support-free printing plans still cannot be guaranteed.

While multi-axis AM holds the potential to effectively reduce the overhang effect, most studies in the topology optimisation area have considered the overhang constraints based on the principles of 3-axis AM. Therefore, to achieve overhang-free designs with good structural performance, a two-step optimisation approach that considers the overhang constraints for multi-axis AM is introduced herein. The proposed approach starts with an optimised design obtained using the traditional topology optimisation. In the first step, to obtain a reliable printing plan (i.e. curved printing surfaces), the design domain is decomposed into a number of zones. Then a new optimisation problem is solved to determine the local build directions for each zone, aiming to maximise the printable proportion of the optimised structure. In the second step, if the proportion of the printable elements is unsatisfactory, a re-optimisation problem is solved to suppress the unprintable elements. With the proposed workflow, both the optimised structure and its associated curved printing surfaces can be identified.

In this paper, previous research on topology optimisation with overhang constraints for 3-axis AM is first reviewed; a new approach based on multi-axis AM is then introduced. Finally, the effectiveness of the proposed approach is evaluated through four case studies, with the relevant findings demonstrating that the sacrifice in performance can be substantially reduced when the proposed workflow is employed.

2. Review of topology optimisation for 3-axis AM overhang constraints

2.1. Review of the traditional solid isotropic material with penalisation approach

The approach proposed in this paper is based on topology optimisation using the Solid Isotropic Material with Penalisation (SIMP) method [39,40], which is briefly reviewed in this section. In the SIMP method, the design domain is discretised into a series of finite elements, with the existence of each element being

determined by the element density $\boldsymbol{\rho}$. The traditional topology optimisation formulation is:

$$\text{find:}\boldsymbol{\rho} = [\rho_1, \rho_2, \ldots, \rho_{n_{\text{ele}}}]^{\mathrm{T}} \tag{1a}$$

$$\text{min: } C = \boldsymbol{F}^T\boldsymbol{U} = \boldsymbol{U}^T\boldsymbol{K}(\boldsymbol{\rho})\boldsymbol{U} = \sum_{i=1}^{n_{\text{ele}}} \boldsymbol{u_i}\boldsymbol{k_i}(\rho_i)\boldsymbol{u_i} \tag{1b}$$

$$\text{s.t.: } \boldsymbol{K}(\boldsymbol{\rho})\boldsymbol{U} = \boldsymbol{F} \tag{1c}$$

$$V(\boldsymbol{\rho}) = \frac{\sum_{i=1}^{n_{\text{ele}}} \rho_i v_i}{\sum_{i=1}^{n_{\text{ele}}} v_i} \leq f \tag{1d}$$

$$0 \leq \rho_i \leq 1, \text{ with } i = 1, 2, \ldots, n_{\text{ele}},$$

where n_{ele} is the number of elements, ρ_i is the density of the ith element (0 for void and 1 for solid), v_i is the volume of the ith element, $V(\boldsymbol{\rho})$ is the volume fraction of the optimised structure, f is the target volume fraction, $\boldsymbol{u_i}$ and $\boldsymbol{k_i}$ are the elemental displacement vector and stiffness matrix respectively, and $\boldsymbol{K}(\boldsymbol{\rho})$, $\boldsymbol{U}$ and $\boldsymbol{F}$ are the structural stiffness matrix, displacement vector and external load vector, respectively.

The Young's modulus E_i for the ith element can be obtained from Equation (2) [41]:

$$E_i = E_{\min} + \rho_i^p(E_0 - E_{\min}), \tag{2}$$

where p is the penalisation factor (typically $p = 3$) used to penalise the Young's modulus values of 'grey' elements (i.e. $0 < \rho_i < 1$), E_0 is the base Young's modulus of the material and $E_{\min}$ is a near 0 parameter used to avoid numerical singularity problems. In addition, element filters are frequently used to address the checkerboard problem, and the Heaviside projection method is used to achieve fully black-and-white solutions. More details on these approaches can be found in [42] and [43].

2.2. Review of 3-axis overhang constraint approach

In this section, the previously established density gradient-based overhang constraint approach for 3-axis AM [26], which serves as the foundation for the approach based on multi-axis AM, is reviewed. This approach incorporates member angle constraints into the topology optimisation problem, so that the incline angles of the structural member boundaries are restricted to avoid the overhang problem illustrated in Figure 1(a). To apply the overhang constraints, the structural overhang parts are first detected by examining the density gradient direction of the boundary elements – see Figure 4; then the overhang elements are eliminated through adding corresponding penalisation to the objection function. For the concerned element i, with its eight neighbouring elements (see Figure 4) having densities equal to ρ_1^i to ρ_8^i, its density gradient direction $\nabla\boldsymbol{\rho_i}$ is given by:

$$\nabla\boldsymbol{\rho_i} = [\alpha_i, \beta_i]^{\mathrm{T}}, \tag{3}$$

where α_i and β_i can be obtained from:

$$\alpha_i = -\frac{1}{6}\rho_1^i + \frac{1}{6}\rho_3^i - \frac{1}{6}\rho_4^i + \frac{1}{6}\rho_5^i - \frac{1}{6}\rho_6^i + \frac{1}{6}\rho_8^i, \tag{4}$$

$$\beta_i = \frac{1}{6}\rho_1^i + \frac{1}{6}\rho_2^i + \frac{1}{6}\rho_3^i - \frac{1}{6}\rho_6^i - \frac{1}{6}\rho_7^i - \frac{1}{6}\rho_8^i. \tag{5}$$

With the density gradient obtained, a boundary element can be defined as self-supporting when its boundary orientation $\boldsymbol{\gamma_i}$, which is perpendicular to the density gradient direction (the blue line shown in Figure 4), lies

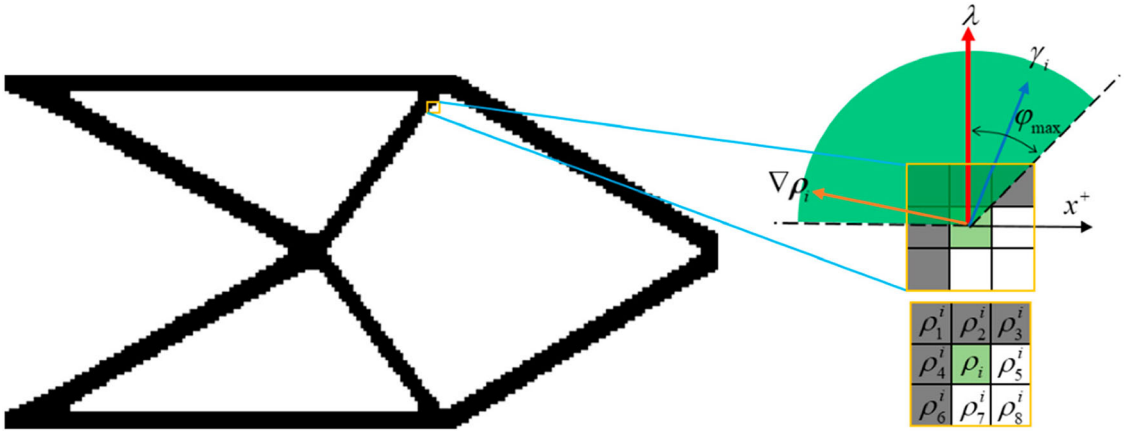


Figure 4. Boundary element i is considered to be self-supportable if its boundary orientation γ_i (i.e. blue arrow) lies within the allowable overhang range (i.e. green region). The red arrow corresponds to the build direction $\boldsymbol{\lambda}$ and the orange arrow represents the density gradient direction $\nabla\boldsymbol{\rho}$.

within the allowable range associated with the build direction (the red line shown in Figure 4), that is:

$$\tau_i = \nabla \boldsymbol{\rho_i} \cdot \boldsymbol{\lambda} - \parallel \nabla \boldsymbol{\rho_i} \parallel \cdot \sin(\varphi_{\max}) < \xi_{i,1}, \tag{6}$$

where τ_i is the overhang value, $\boldsymbol{\lambda}$ is the build direction and ξ_{i1} is a near 0 parameter used to avoid numerical problems.

The explicit overhang angle constraint for the ith element can now be formulated as follows:

$$\frac{\sum_{i=1}^{n_{\text{ele}}} \omega_i v_i \rho_i}{\sum_{i=1}^{n_{\text{ele}}} v_i} \leq 0, \tag{7}$$

where ω_i can be expressed as:

$$\omega_i = h(\tau_i - \xi_{i,1}) \tag{8}$$

$$= \frac{1}{1 + e^{-2\mu(\tau_i - \xi_{i,1})}}, \tag{9}$$

in which $h()$ is a step function used to transform the values of overhang violation $\tau_i - \xi_{i,1}$ into ω_i with near binary value; μ is a parameter that indicates the smoothness of the step function and usually lies between 35 and 50.

It is worth noting that in the previous literature, there exist two types of methods in addressing the overhang problem: layer-by-layer methods [22] and density gradient-based methods [26]. While the former considers the support relation between elements, the latter focus on restricting the structural member orientations. Since the support relation is not considered in the density gradient-based approach, it is susceptible to a so-called 'hanging feature' problem, which may yield icicle-shaped structural parts that are satisfied with the overhang angle constraint but not supported by surrounding elements. To address this problem, another hanging feature constraint needs to be utilised. Details about this approach can be found in [26].

3. Overhang constraints based on multi-axis AM

In this section, the 3-axis overhang constraint approach is extended to cater for the characteristics of multi-axis AM. While the structure is the only design object in 3-axis AM, both the structure and the corresponding printing plan must be determined for multi-axis AM. The following two-step approach is therefore proposed:

- In the first step (described in Section 3.1), an optimised structure, determined using traditional topology optimisation, is used as the starting point. The design domain is then decomposed into a number of zones, with each zone being assigned one local build direction. Subsequently, the local build directions are determined by assessing the boundary element orientation within each zone, targeting the achievement of the maximum printable proportion of the optimised structure. Note that in this step, the layout of the optimised structure is kept constant.
- If the unprintable ratio (i.e. the proportion of unprintable boundary elements) is less than a target threshold r_t, which is customised by the requirement of manufacturing, the algorithm terminates; otherwise, a subsequent step, termed re-optimisation (described in Section 3.2), is carried out to modify the shape of the structure such that the number of overhang elements can be eliminated.

3.1. Printing plan optimisation for a given structure

As illustrated in Figure 2, multi-axis printing allows different local printing directions to be used during the printing process. To mimic this feature, the design domain is divided into a number of zones, and it is assumed that each zone corresponds to one fixed build direction only. Subsequently, linear programming is employed to identify the build directions, targeting the achievement of the maximum printable proportion of the structure. Note that in our approach, we presume the structure is constructed from bottom zone layers to the top, with the printing surfaces aligning perpendicularly to the respective local build directions within each zone. Based on this assumption, continuous printing surfaces for each individual layer can be obtained, utilising the specific build directions within that zone layer. The further generated tool paths based on the printing surfaces can be adopted by the multi-axis printer such as the WAAM printer. The domain subdivision approach is introduced in Section 3.1.1, while the printing plan optimisation is described in Sections 3.1.2–3.1.5.

3.1.1. Domain subdivision

For subdividing the domain, the simplest method employs a rectangular grid with uniform spacing, hereafter referred to as the 'regular grid approach' (see Figure 5(a)). Although this strategy can be applied in problems with all range of volume fractions, it is more inclined to yield satisfactory results for problems with medium to high volume fractions (e.g. $f \geq 0.5$). This is potentially because high volume fractions result in less void volume in the given design domain, making the problem less susceptible to the overhang effects. In addition, it is worth noting that the zone arrangement

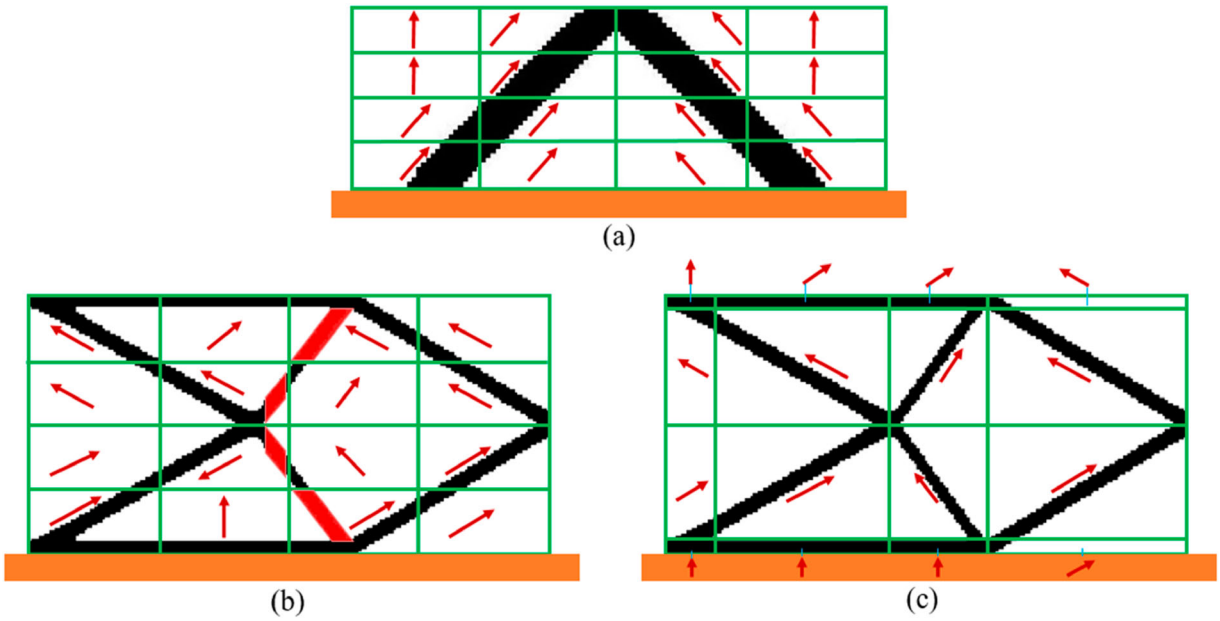


Figure 5. Design domain subdivision: (a) structure that can be fully printed using equal-sized zones (i.e. regular grid approach); (b) structure with simple geometry, with equal-sized zones making part of the structure unprintable (i.e. marked in red); (c) simple structure that can be fully printed using customised zones; red arrows represent the local build directions.

that can lead to an approximately 100% printable structure is not unique; in general, smaller grid size can lead to a more ideal solution (i.e. lower performance sacrifice). However, the grid size should be no less than a minimum threshold which depends on the multi-axis equipment. The effect of different zone arrangements is discussed further in Section 4.3.

For problems with lower volume fractions (e.g. $f = 0.2$ as in Figure 5(b)), the regular grid approach tends to produce a lower proportion of printable structures. This issue arises because, for a structural component to be printable, its boundary orientation must fall within the printable range relative to the build direction, as depicted in Figure 4. If a single zone contains two or more members with significantly different orientations, it is not possible to ascertain a single build direction that guarantees printability for all members. To address this issue, one could customise the positions of zone boundaries, ensuring that all members within a given zone possess similar orientations (see Figure 5(c)).

Nevertheless, low volume fraction problems often result in truss-like structures (e.g. Figures 6). This makes it possible to position the split lines at the joint positions, thereby achieving desirable zone arrangements (i.e. joint-split approach). In this study, the structural corner positions are first identified using the Harris Corner Detection approach [44] – see Figure 6 (a). The zone boundaries are then added to the identified corner positions, such that the structure is subdivided with the members with different orientations being separated into different zones – see Figure 6(b). It is worth noting that for non-truss-like structures, the

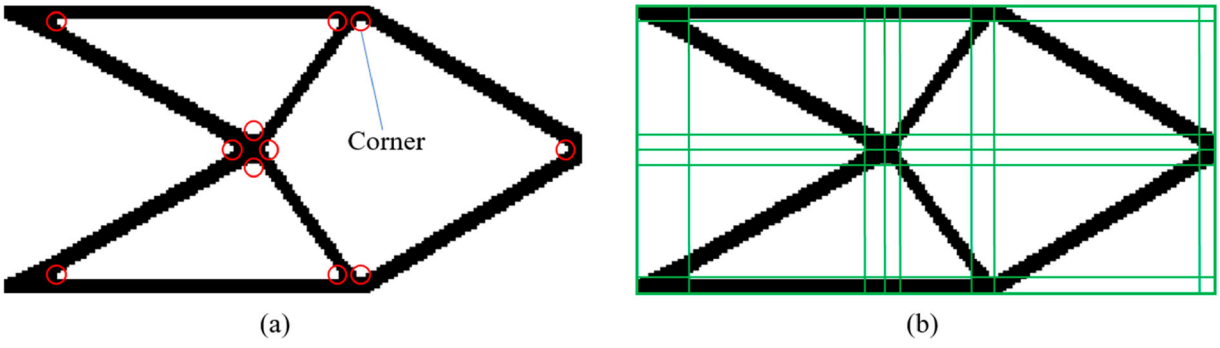


Figure 6. Domain subdivision based on structural corner locations (i.e. joint-split approach); (a) structural corners; (b) zone boundaries.

joint-split approach cannot guarantee satisfactory results due to inconspicuous corners. Therefore, the joint-split approach works optimally when the volume fraction is relatively low and the structure is truss-like. In fact, only the low volume fraction problems require the joint-split approach as they are more susceptible to the overhang effect, which necessitates the use of customised zone arrangements.

3.1.2. Determination of build direction in each zone

After the domain subdivision step, the local build direction of each zone φ_j, as shown in Figure 7, is determined by assessing the structural member orientation within each zone. Similar to the approach used for a 3-axis configuration, as described in Section 2.2, a structure can be considered to be fully printable when all the boundary elements are self-supporting. Since the target structure is fixed during this step, the density gradients of all boundary elements are known constants. Therefore, the corresponding boundary orientation $\bar{\varphi}_i$ for the ith element can be obtained from:

$$\bar{\varphi}_i = \begin{cases} \varphi_{i,g} + \dfrac{\pi}{2}, & \text{if } 0 \le \varphi_{i,g} \le \dfrac{\pi}{2} \\ \varphi_{i,g} - \dfrac{\pi}{2}, & \text{if } \dfrac{\pi}{2} \le \varphi_{i,g} \le \dfrac{3}{2}\pi \\ \varphi_{i,g} - \dfrac{3}{2}\pi, & \text{if } \dfrac{3}{2}\pi \le \varphi_{i,g} \le 2\pi \end{cases}, \quad (10)$$

where $\varphi_{i,g}$ is the gradient orientation of element i (i.e. the angle between the $\nabla\boldsymbol{\rho}_i$ and x^+ in Figure 4).

If a boundary element i in zone j satisfies the following equation:

$$|\varphi_j - \bar{\varphi}_i - \varphi_{\max}| + |\varphi_j - \bar{\varphi}_i + \varphi_{\max}| = 2\varphi_{\max}, \quad (11)$$

boundary element i is determined to be printable. Note that if a boundary element is not self-supporting, the left-hand side of Equation (11) becomes greater than the right-hand side, causing an overhang violation. Therefore, to maximise the printable proportion of a structure, the following optimisation problem can be solved:

$$\text{find: } \boldsymbol{\varphi} = [\varphi_1,\ \varphi_2,\ \ldots \varphi_{n_z}]^{\mathrm{T}} \quad (12a)$$

$$\min: P = \boldsymbol{O}^T \boldsymbol{\eta} \quad (12b)$$

$$\text{s.t.: } \boldsymbol{O} = |\boldsymbol{M}\boldsymbol{\varphi} - \bar{\boldsymbol{\varphi}} - \varphi_{\max}| + |\boldsymbol{M}\boldsymbol{\varphi} - \bar{\boldsymbol{\varphi}} + \varphi_{\max}|, \quad (12c)$$

where P is the total overhang violation of the optimised structure; $\boldsymbol{O} = [O_1,\ O_2,\ \ldots O_i,\ \ldots O_{n_{\text{ele}}}]^{\mathrm{T}}$ is the element overhang violation vector, with O_i denoting the overhang violation of the ith element; $\boldsymbol{\eta} = [\eta_1,\ \ldots \eta_i,\ \ldots \eta_{n_{\text{ele}}}]^{\mathrm{T}}$, with $\eta_i = 1$ for the boundary elements and $\eta_i = 0$ for all other elements, $\boldsymbol{M}$ is a 0–1 mapping matrix used to obtain the corresponding zone of each element, $\boldsymbol{\varphi} = [\varphi_1,\ \varphi_2,\ \ldots,\ \varphi_{n_z}]^{\mathrm{T}}$ is the local build direction vector, with n_z denoting the number of zones and $\bar{\boldsymbol{\varphi}} = [\bar{\varphi}_1,\ \bar{\varphi}_2,\ \ldots,\ \bar{\varphi}_{n_{\text{ele}}}]^{\mathrm{T}}$ is the elemental incline angle vector.

3.1.3. Collision between the printing nozzle and the structure

In multi-axis AM, the printing nozzle and the already printed component may collide, if a rapid change in local build direction occurs between two adjacent zones and yields a deep concave printing surface (e.g. Figure 3(a)). To avoid this problem, the following constraint can be used to restrict the turning angle of the printing surfaces:

$$\varphi_{\text{next}} - \varphi_{\text{first}} < \varphi_{\text{t, max}}, \quad (13)$$

where φ_{next} and φ_{first} are the build directions of two adjacent zones (see Figure 8), and $\varphi_{\text{t,max}}$ is the maximum turning angle.

It is worth noting that for printing nozzles with a relatively sharp shape, the risk of collision is reduced, allowing for a relatively high $\varphi_{\text{t, max}}$. Conversely, a blunt-shaped nozzle necessitates a lower $\varphi_{\text{t, max}}$. When $\varphi_{\text{t, max}} = 0$, the printing surfaces can only be horizontal or convex, ensuring collision-free printing process for printing nozzles with arbitrary shapes. The effects of different

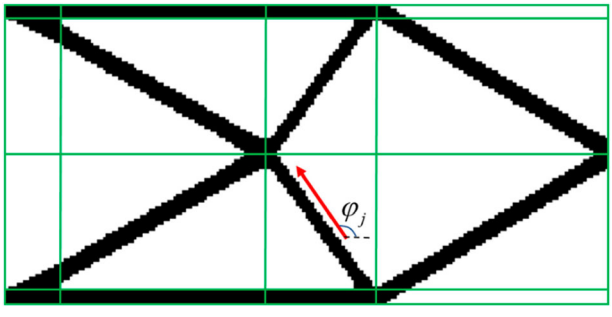


Figure 7. Local build direction φ_j of zone j.

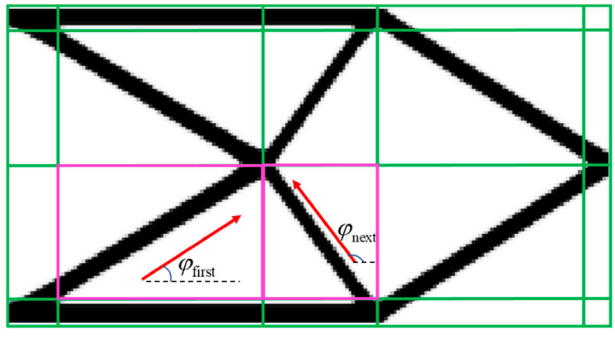


Figure 8. Local build directions φ_{first} and φ_{next} of two adjacent zones.

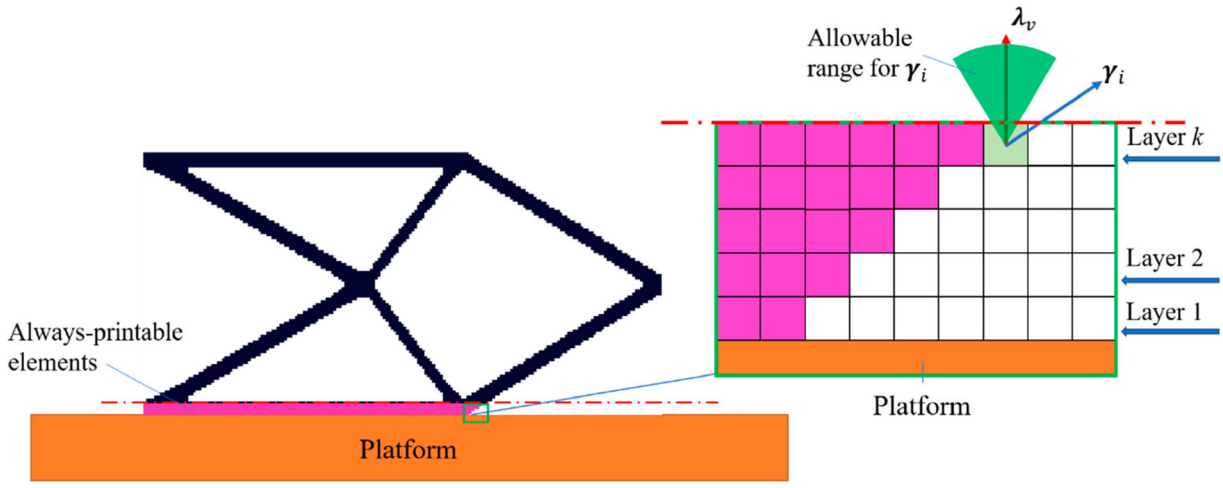


Figure 9. Identification of elements that can be built vertically from the base platform.

$\varphi_{t,\ max}$ values on the optimisation result are discussed later in Section 4.5. Note that Constraint (13) offers a simplified method to minimise the risk of collision during the structural design phase, while maintaining low computational costs. For a comprehensive elimination of collision risks, a thorough collision assessment can be performed in the detail path planning stage [10].

3.1.4. Consideration of definitively printable elements

There are two types of structural elements that are definitively printable, irrespective of the constraints described in the previous sections: (1) those that can be built vertically directly from the base platform and (2) those that are supported by neighbouring elements across all the base platform orientations.

The first type of these elements is illustrated in Figure 9. While the highlighted elements would be defined as overhanging due to their horizontal boundary orientation, they can be printed using a vertical build direction since they are directly attached to the base platform. To identify this type of element, a scanning process is conducted, as illustrated in Figure 9, where a vertical build direction $\boldsymbol{\lambda}_v$ is used to evaluate the printability of each element using the following constraint:

$$\tau_{i,v} = \nabla\boldsymbol{\rho_i} \cdot \boldsymbol{\lambda}_v - \parallel \nabla\boldsymbol{\rho_i} \parallel \cdot \sin(\varphi_{\max}) \leq \delta, \qquad (14)$$

where δ is a near 0 tolerance used to avoid numerical errors and $\tau_{i,v}$ is the overhang violation value for the ith element. The scan process starts from the first layer of elements that are directly attached to the base platform and ends when the first unprintable element emerges; and the end layer is identified as the kth layer. All elements below the kth layer are definitively printable and are thus excluded from Equation (12) by assigning them a value of $\eta = 0$.

The second type of definitively printable elements are those consistently supported by neighbouring elements across all base platform orientations, as demonstrated in Figure 10. These elements satisfy the following condition:

$$\beta_i \leq \sigma|\alpha_i| \qquad (15)$$

where α_i and β_i are the density gradient components defined in Equations (4) and (5); σ can be determined from:

$$\sigma = -\tan(\varphi_{\text{allow}} - \varphi_{\max}), \qquad (16)$$

where φ_{allow} is the allowable rotation angle of the platform; in this study $\varphi_{\text{allow}} = \frac{\pi}{2}$ is used.

It is important to note that Constraint (15) differs mathematically from Constraint (11). While the former is a non-linear constraint, the latter is linear. Moreover, Constraint (15) encompasses a wider optimisation search region compared to Constraint (11). This is because, for each structural member, there exist two possible directions, for example $\overrightarrow{AB}$ and $\overrightarrow{BA}$ in Figure 10. An element is overhang free if one of $\overrightarrow{AB}$ and $\overrightarrow{BA}$ satisfies the overhang angle constraint (11). For example, in Figure 10(a), the target element is supported by the elements located on the point A side, thus $\overrightarrow{AB}$ satisfies Constraint (11); in Figure 10(b–e), the target element is supported by elements located on the point B side, thus $\overrightarrow{BA}$ satisfies Constraint (11). However, in the optimisation we preselect the vector $\overrightarrow{BA}$ via the piecewise function (10) (i.e. based on the 0° base platform orientation). While this preselection greatly reduces the numerical complexity and makes Constraint (11) linear, it may potentially restrict the search region of the optimisation problem, impacting the quality of the solutions. Therefore, to address this

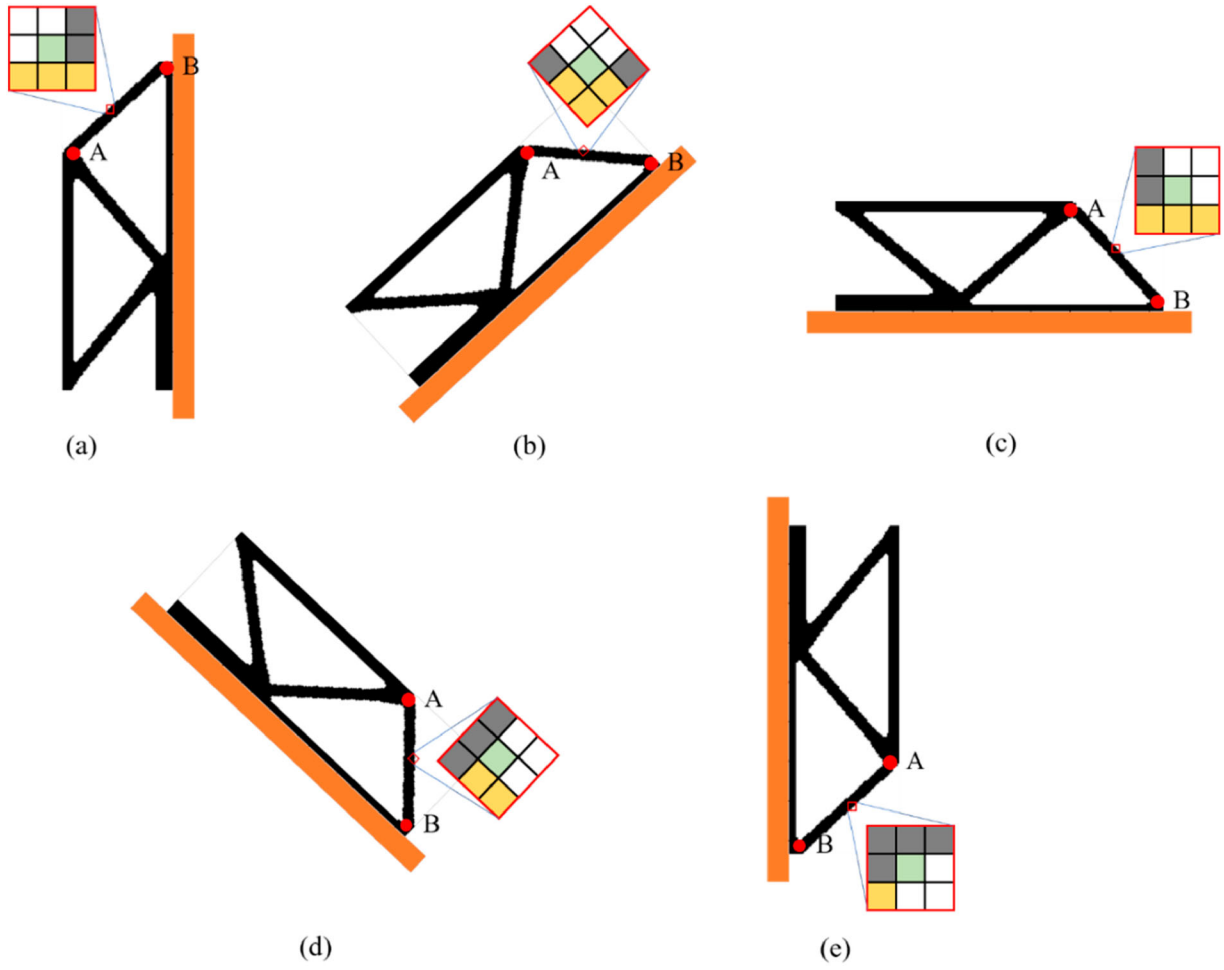


Figure 10. The target element (highlighted by green) can be supported by neighbouring elements (highlighted by yellow) for all base platform orientations within $[-90^\circ, 90^\circ]$: (a) -90° base platform orientation; (b) -45° base platform orientation; (c) 0° base platform orientation; (d) 45° base platform orientation; (e) 90° base platform orientation; a maximum overhang angle $\varphi_{\max} = 45^\circ$ is utilised in this example.

problem, the nonlinear Constraint (15), which accommodates both $\overrightarrow{AB}$ and $\overrightarrow{BA}$ directions, is utilised to exclude the second type of definitively printable elements from the optimisation problem, thereby improving printable ratio of the optimised solutions.

3.1.5. Optimisation of local printing directions

By combining Equations (12) and (13), the following optimisation problem can be solved to obtain the build directions of all the printing zones:

$$\text{find}: \boldsymbol{\varphi} = [\varphi_1, \varphi_2, \ldots, \varphi_{n_z}]^{\mathrm{T}} \tag{17a}$$

$$\min: P = \boldsymbol{O}^{\mathrm{T}}\boldsymbol{\eta} \tag{17b}$$

$$\text{s.t.}: \boldsymbol{O} = |\boldsymbol{M}\boldsymbol{\varphi} - \bar{\boldsymbol{\varphi}} - \varphi_{\max}| + |\boldsymbol{M}\boldsymbol{\varphi} - \bar{\boldsymbol{\varphi}} + \varphi_{\max}| \tag{17c}$$

$$\boldsymbol{\varphi}_{\text{next}} - \boldsymbol{\varphi}_{\text{first}} < \varphi_{\text{t,max}}, \tag{17d}$$

where $\boldsymbol{\eta} = [\eta_1, \ldots \eta_i, \ldots \eta_{n_{\text{ele}}}]^{\mathrm{T}}$ with $\eta_i \in \{0, 1\}$ and $\eta_i = 1$ for the boundary elements that are not 'definitively printable' and $\eta_i = 0$ for all other elements. Since the objective function and the constraints are linear, the optimisation problem expressed by Equation (17) is a linear programming problem which can be efficiently solved using interior point solvers, such as *MOSEK* [45], with the optimised solutions guaranteed to be the global optimum.

3.2. Re-optimisation

Although the optimisation problem expressed by Equation (17) can identify the local build directions that render the target structure as printable as possible, it does not guarantee the full printability of any arbitrary structure. Therefore, a structure re-optimisation is carried out to suppress the unprintable elements when their proportion r_{unp} exceeds the target value r_{t}. In this step, we treat the overhang constraints in each individual zone as if in the 3-axis AM (e.g. Constraint (6)). The only difference

is that the previous vertical build direction utilised in 3-axis AM is replaced by the multi-axis AM local build directions (i.e. $\boldsymbol{\varphi}$) obtained from solving Equation (17).

By integrating the local build direction into the topology optimisation problem, the formulation for the re-optimisation is given by:

$$\text{find: } \boldsymbol{\rho} = [\rho_1, \rho_2, \ldots, \rho_{n_{\text{ele}}}]^{\text{T}} \tag{18a}$$

$$\min: C(\boldsymbol{\rho}) = \boldsymbol{F}^T\boldsymbol{U} = \boldsymbol{U}^T\boldsymbol{K}(\boldsymbol{\rho})\boldsymbol{U} \tag{18b}$$

$$\text{s.t.:} \boldsymbol{K}(\boldsymbol{\rho})\boldsymbol{U} = \boldsymbol{F} \tag{18c}$$

$$\frac{\sum_{i=1}^{n_{\text{ele}}} v_i\rho_i}{\sum_{i=1}^{n_{ele}} v_i} \leq f \tag{18d}$$

$$\frac{\sum_{i=1}^{n_{\text{ele}}} \omega_i(\varphi_j)v_i\rho_i}{\sum_{i=1}^{n_{ele}} v_i} \leq 0 \tag{18e}$$

Note that, in multi-axis AM, for the ith element in the jth zone, ω_i can be calculated by:

$$\omega_i(\varphi_j) = h(\nabla\boldsymbol{\rho}_i \cdot \boldsymbol{\lambda}(\varphi_j) - \parallel \nabla\boldsymbol{\rho}_i \parallel \cdot \sin(\varphi_{\max}) - \xi_{i,1}), \tag{19}$$

where φ_j is the build direction of element i in the jth zone, and the corresponding build direction vector $\boldsymbol{\lambda}(\varphi_j) = (\cos(\varphi_j), \sin(\varphi_j))$.

It is worth noting that although we adopt the density gradient-based approach that is reviewed in Section 2.2, we do not consider the hanging feature constraint [26] in the re-optimisation Equation (18). This is because the optimisation problem with multi-axis AM is less prone to the hanging feature problem. To elaborate, previously in 3-axis AM, when the angle constraint is applied, the structure undergoes a significant change in the overall layout (i.e. compared to the results obtained without overhang constraints). Consequently, icicle-shaped hanging parts may emerge during the optimisation process. However, in multi-axis AM, due to the extreme printing flexibility provided, the structure only undergoes minor change compared to the results from the traditional topology optimisation approaches. Consequently, the hanging feature rarely appears. This is evident in all the examples shown in Sections 4.

3.3. Summary

For sake of clarity, a flow chart for the proposed two-step algorithm is presented in Figure 11. Note that at the end of Step 2, the volume-preserving Heaviside projection [42] is applied to obtain full black-and-white solutions.

4. Numerical examples

In this section, four numerical examples are presented to demonstrate the effectiveness of the proposed approach. The Young's modulus E_0 and Poisson's ratio

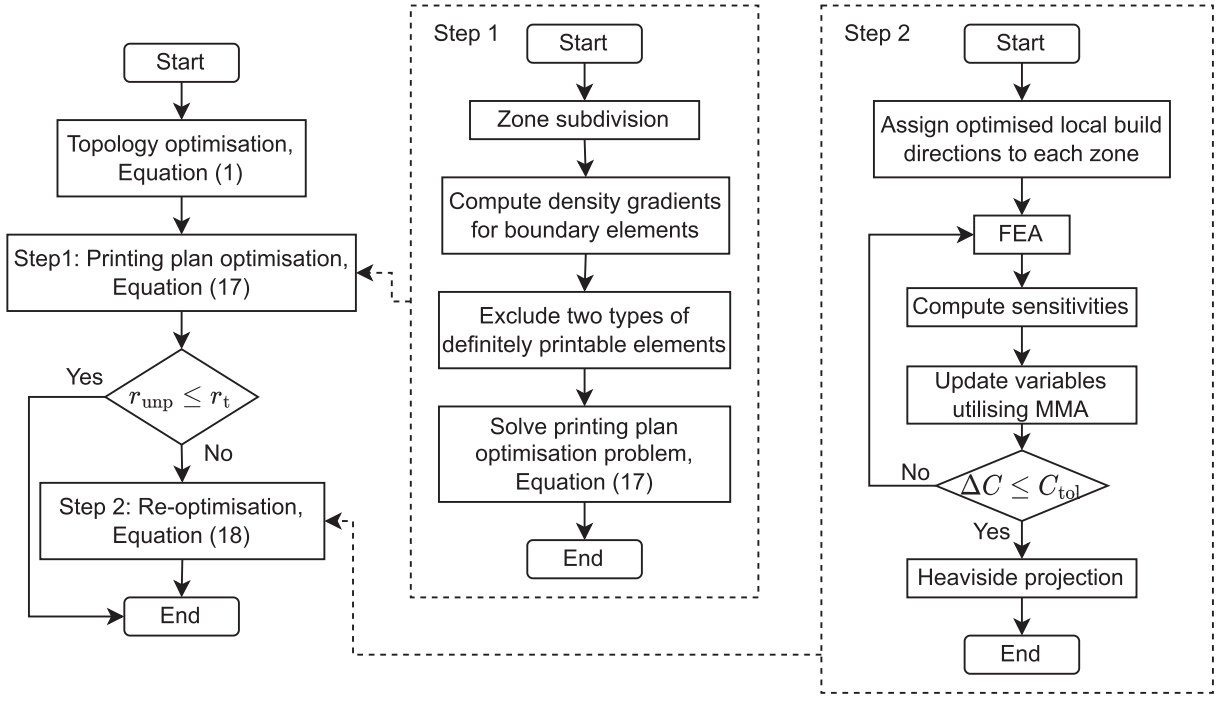


Figure 11. Algorithm flow chart, where r_{unp} and r_{t} denote the printable ratio of the optimised structure and the target printable ratio, respectively; $\Delta C = |(C_t - C_{t-1})/C_t|$ represents the change in compliance between the two adjacent iterations, with t denoting the iteration index; C_{tol} is the convergence tolerance.

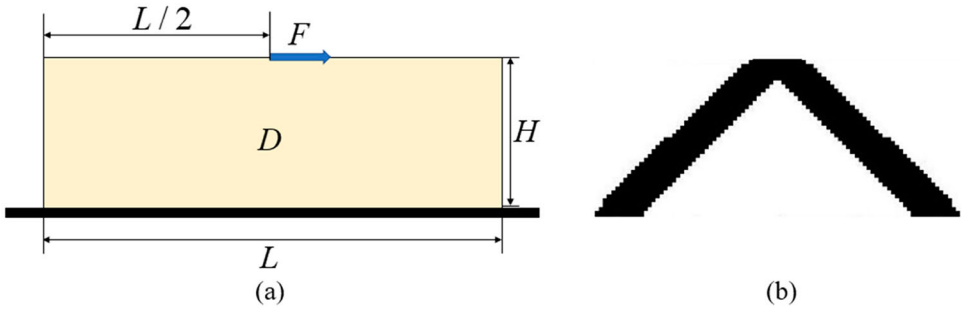


Figure 12. Two-bar example: (a) design domain, load and support conditions; (b) solution obtained using traditional topology optimisation; the structural compliance $C = 7.94$ N mm.

v are assumed to be 1.0 N/mm^2 and 0.3, respectively, the minimum Young's modulus E_{min} is 1×10^{-9} N/mm^2 and the penalty parameter p is taken as 3. All design domains are meshed using quadrilateral elements. The maximum tilting angle for the base platform φ_{allow} is taken as 90° (used in Equation (16)), while the maximum turning angle $\varphi_{t,max}$ is $\frac{\pi}{2}$. Finally, the unprintable threshold r_t (i.e. used to judge whether the re-optimisation step should be carried out) is taken as 1% and $C_{tol} = 0.1\%$ is utilised in the re-optimisation. All the examples in this section are coded in Python, and CPU times are obtained using a laptop equipped an Intel Core i7-9750H CPU.

4.1. Simple two bar structure

The process of the proposed approach is first demonstrated through a simple two-bar structure shown in Figure 12(a), where F is a unit load, $L = 120$ mm and $H = 40$ mm are the dimensions of the design domain and the volume fraction $f = 0.2$. The optimised solution from the traditional SIMP method is shown in Figure 12 (b). In 3-axis AM, the two structural members are not supported at the bottom boundaries (see Figure 12(b)) when $\varphi_{max} = 0$; multi-axis AM can be therefore used to improve printability.

The structure shown in Figure 12(b) constitutes the starting point of the printing plan optimisation approach. Firstly, the optimised structure is divided into four zones, using the joint-split approach described in Section 3.1 – see Figure 13(a). Then the 'definitively printable' elements are identified using the method introduced in Section 3.1.4 and excluded from the optimisation problem – see Figure 13(b). The optimisation problem expressed by Equation (17) is then solved for the determination of the local build directions, as shown in Figure 13(c). With the local build directions determined, the printing surfaces can be constructed, being orthogonal to the build directions. At this stage, 97.5% of the structure is printable and the elements that violate the overhang constraint are highlighted in white in Figure 13(d). Since r_{unp} is greater than the threshold $r_t = 1.0\%$, the re-optimisation step described in Section 3.2 is carried out to reduce the unprintable proportion. The obtained solution is shown in Figure 13(e) and (f), where r_{unp} is reduced to 0 and the associated compliance increase is 2.1% (i.e. compared to the benchmark shown in Figure 12(b)).

Note that Garaigordobil et al. [24] previously studied the same 2-bar structure in a 3-axis AM context and their optimised result is reproduced in the present paper by using a single zone and by setting the printing direction to 90°. The obtained structure, illustrated in Figure 14, has a similar topology to that presented in [27], and is associated with a 140.3% compliance increase relative to Figure 12(b). Comparing Figure 14 to Figure 13(e), the compliance increase caused by the overhang constraint is reduced from 140.3% to 2.1% by switching from 3-axis to multi-axis AM, highlighting the superiority of the proposed approach.

4.2. MBB beam

In this section, we examine a Messerschmitt-Bölkow-Blohm (MBB) beam using the regular grid approach detailed in Section 3.1.1. Figure 15(a) presents the case description, where we consider only half of the beam due to its symmetry. The maximum overhang angle $\varphi_{max} = 45°$. The design domain is specified with a length (L) of 240 mm and a height (H) of 80 mm; the magnitude of the load (F) is 0.5 N and the volume fraction (f) is assigned a value of 0.5. Figure 15(b) depicts the optimised result from the traditional topology optimisation approach, yielding a structural compliance $C = 46.71$ N mm.

The results of MBB beam are shown in Figure 16. Initially, upon employing the 3-axis AM approach, the unprintable ratio r_{unp} for Figure 15(b) is 20.14%. After utilising optimised multi-axis AM printing plan as shown in Figure 16(c), r_{unp} is reduced to 5.04%. Further re-optimisation reduces r_{unp} to 0.0%, with only a modest 3.08%

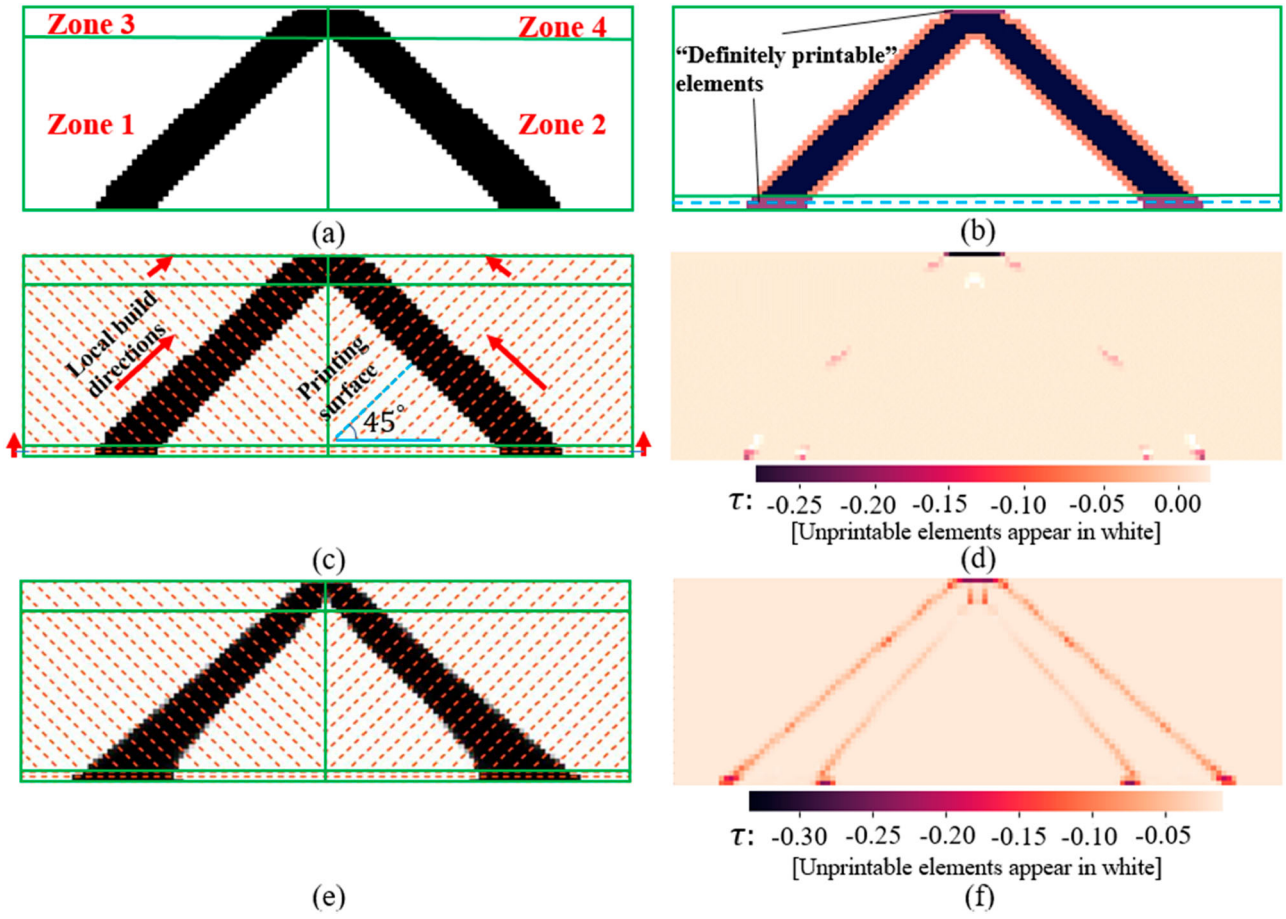


Figure 13. Steps of the proposed optimisation approach for a two-bar structure: (a) zone subdivision; (b) identification of definitively printable elements that are not considered in the printing plan optimisation (coloured in purple) and boundary elements (coloured in orange) that are considered in the printing plan optimisation; (c) optimised local build directions. ($r_{unp} = 2.5\%$); (d) elemental overhang violation value τ for the structure in (c); (e) optimised solution after the re-optimisation. ($r_{unp} = 0.0\%$ and structural compliance $C = 8.11$ N mm); (f) elemental overhang violation value τ for the structure in (e); orange dashed lines represent printing surfaces; red arrows represent the local build directions; C denotes the structural compliance; r_{unp} represents the unprintable element proportion, and the unprintable elements have $\tau = 0$, which are coloured in white in (d) and (f).

increase in compliance compared to the nominal design in Figure 15(b). A convergence history of the re-optimisation step is shown Figure 17, it's worth noting that r_{unp} remains low (i.e. $\leq 0.2\%$) throughout the convergence process. Although r_{unp} lacks physical significance in the initial stages (since the optimised structure isn't fully binary), it sees a minor increase in the later stages as the structure gradually solidifies into a black-and-white structure. Nevertheless, this is swiftly countered by the imposition of the overhang constraint (18e), effectively reducing r_{unp} to zero at the final convergence.

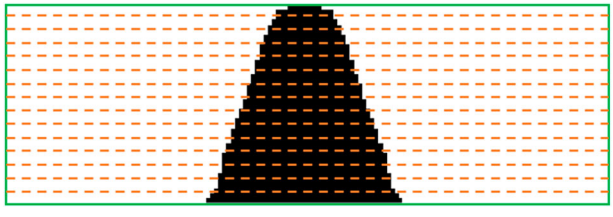


Figure 14. Self-supporting solution for 3-axis AM (C = 19.08 N mm).

4.3. Influence of maximum overhang angle

The overhang angle tolerance φ_{max} is a crucial parameter for AM, with its value depending on the material being printed and the adopted AM method. To investigate its influence on the optimised results, the MBB beam example introduced in Section 4.2 is studied for a range of different φ_{max} values. The volume fraction f is taken as 0.25, and the rest parameters are the same as 4.2. The zone arrangement utilised by the printing plan optimisation is shown in Figure 18(b), with the considered φ_{max} values being 60°, 45° and 30°.

As discussed in Section 3.1.1, for problems with low volume fractions, we employ the joint-split approach to

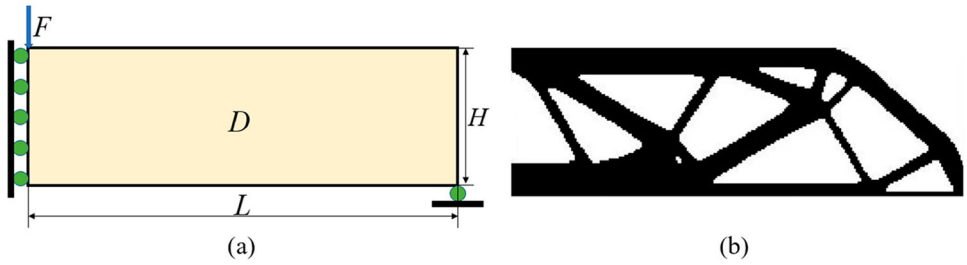


Figure 15. MBB example when volume fraction is 0.5; (a) design domain, load and support conditions; (b) solution obtained using traditional topology optimisation; the structural compliance $C = 46.71$ N mm.

achieve a customised zone arrangement. The optimised results for the different φ_{max} values are shown in Figure 19(a) and (b), with the unprintable ratios r_{unp} being 0.25%, 0.75%, 0.98% for $\varphi_{max} = 60^\circ$, 45° and 30°, respectively, which confirms that joint-split approach can achieve high printable proportions. The fact that r_{unp} was found to increase with decreasing φ_{max} suggests that in situations with low φ_{max} values, the structures are more challenging to print. Note that the printing difficulty caused by low φ_{max} values is also evident in the reduction in definitively printable elements, as shown in Figure 19(a), where it can be observed that the top boundary elements of the inclined structural members change from being definitively printable to

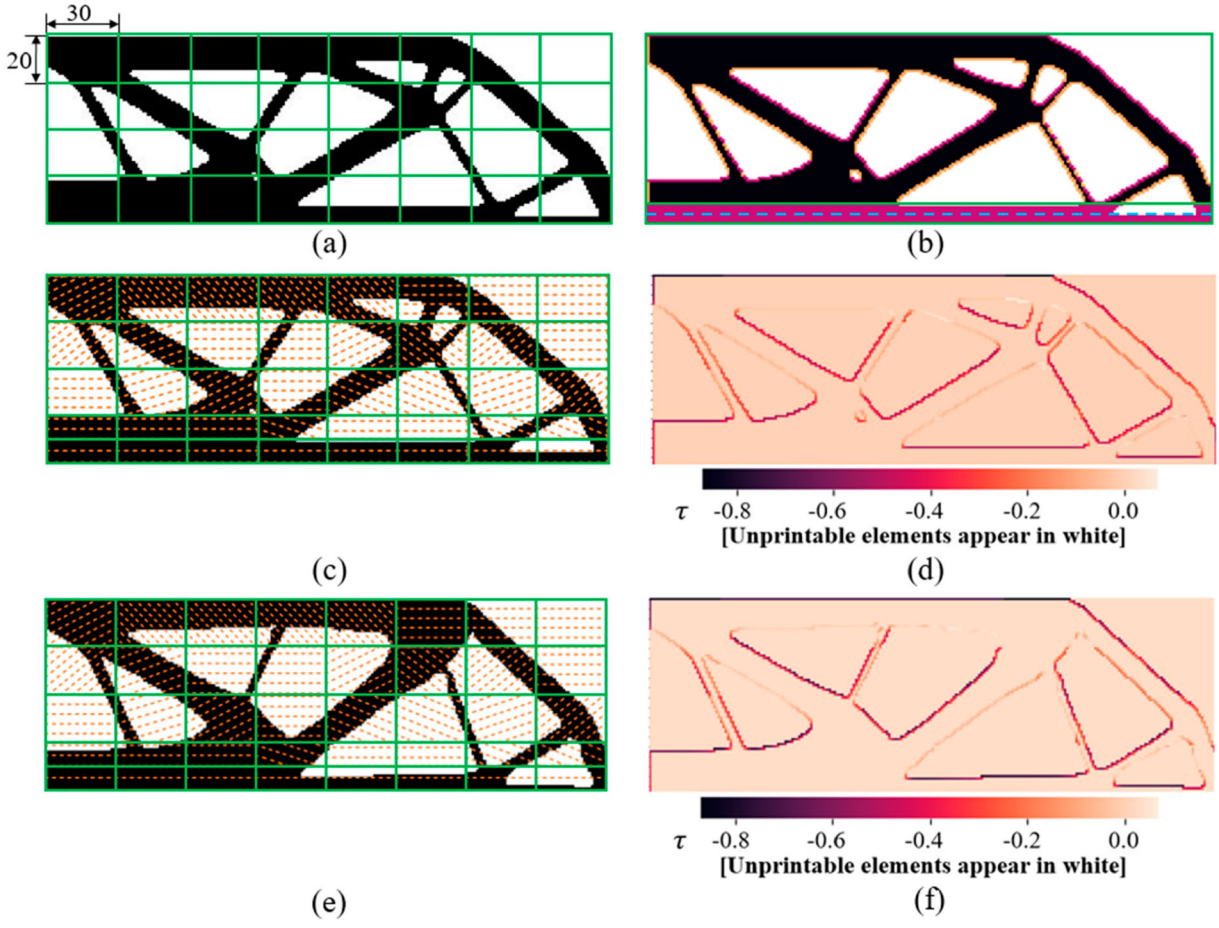


Figure 16. Steps of the proposed optimisation approach for a MBB beam: (a) zone subdivision; (b) identification of definitively printable elements that are not considered in the printing plan optimisation (coloured in purple) and boundary elements that are considered in the printing plan optimisation (coloured in orange); (c) optimised local build directions. ($r_{unp} = 5.04\%$); (d) elemental overhang violation value τ for the structure in (c); (e) optimised solution after the re-optimisation. ($r_{unp} = 0.0\%$ and structural compliance $C = 48.15$ N mm); (f) elemental overhang violation value τ for the structure in (e); orange dashed lines represent printing surfaces; red arrows represent the local build directions; C denotes the structural compliance; r_{unp} represents the unprintable element proportion, and the unprintable elements have $\tau = 0$, which are coloured in white in (d) and (f).

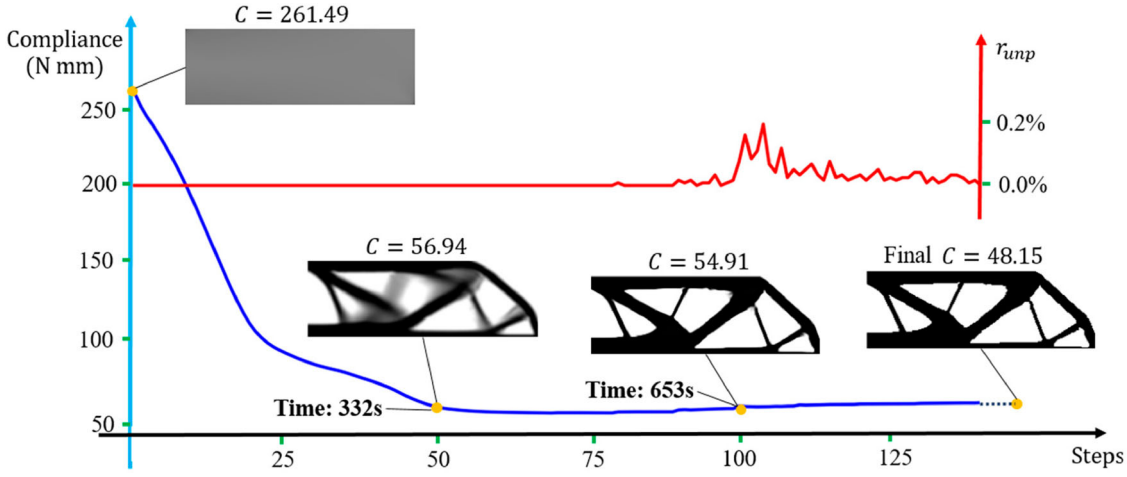


Figure 17. Convergence history and computational time of the re-optimisation step for the MBB beam in Figure 16(e).

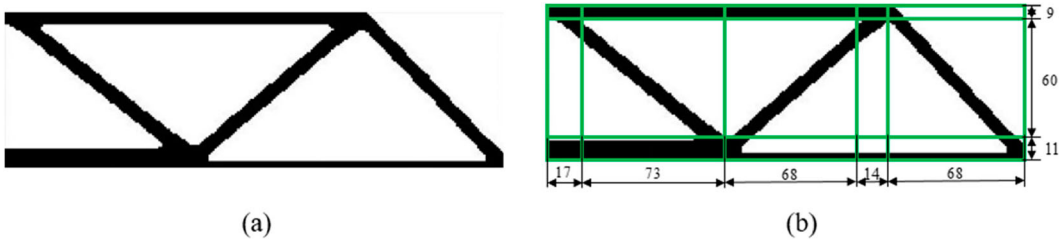


Figure 18. MBB beam example when $f = 0.25$: (a) solution obtained using traditional topology optimisation, with dimensions in mm (structural compliance $C = 85.45$ N mm); (b) zone arrangements determined from the joint-split approach.

non-definitively printable as φ_{max} decreases from 60° to 30°. Nevertheless, since in three examples the printable ratios are all large than 99.0% and $r_{unp} < r_t$ is satisfied, the re-optimisation is not carried out in this example.

The printing process for the printing plan shown in Figure 19(b-2) can be illustrated by Figure 20. Initially, the base platform is positioned horizontally for the first few layers (Figure 20(a)), and then, the printing nozzle moves along the printing path layer by layer (Figure 20(b) and Figure 20(c)). For the sake of completeness, the elemental overhang violation for Figure 19(a-2) is shown in Figure 21.

Gaynor et al. [22] investigated the same MBB example for 3-axis AM and for $\varphi_{max} = 45°$, with the corresponding compliance increase caused by the overhang constraints based on 3-axis AM being 20.6%. Using the

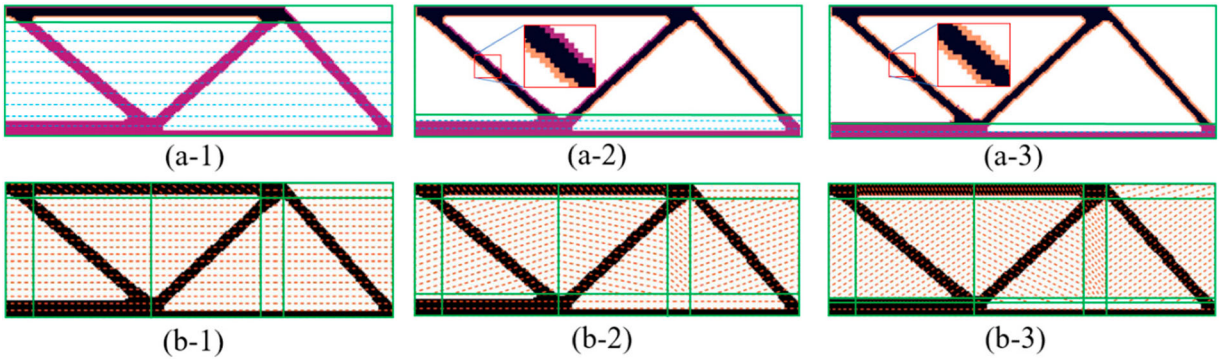


Figure 19. Optimised results of MBB example: (a) definitively printable elements that are not considered in the printing plan optimisation (coloured in purple) and boundary elements that are considered in the printing plan optimisation (coloured in orange); (b) optimised solutions for multi-axis printing when the maximum overhang angle φ_{max} is (1) 60°; (2) 45°; (3) 30°; orange dashed lines represent printing surfaces.

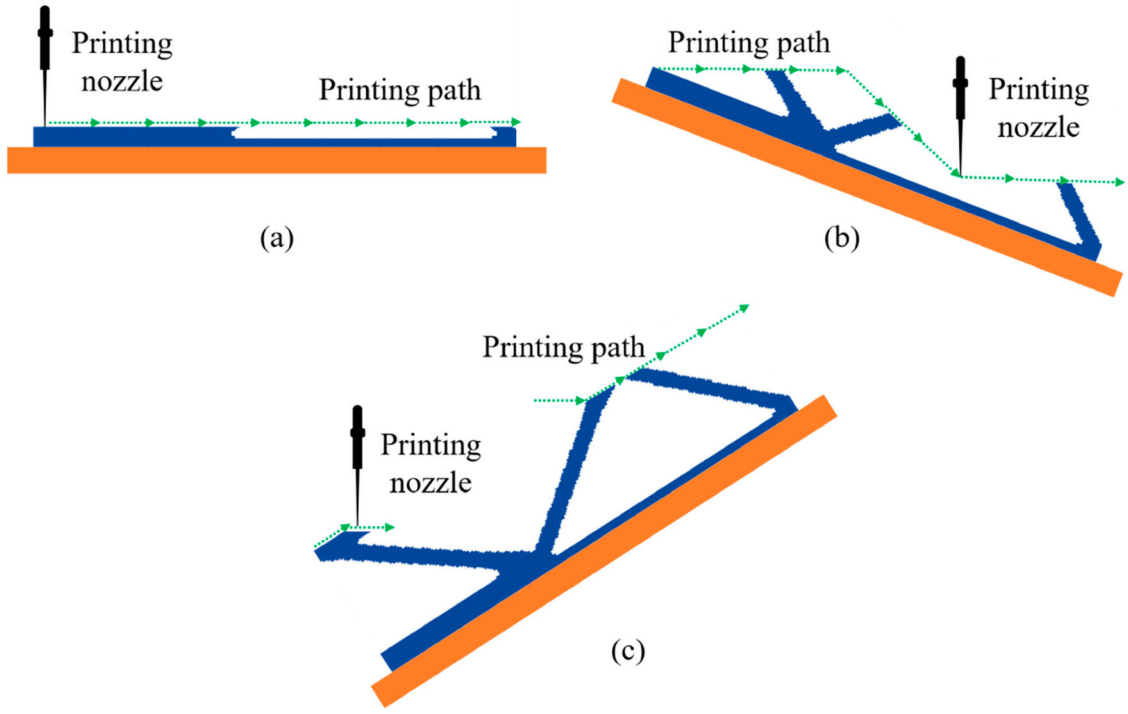


Figure 20. Procedure of multi-axis printing for MBB beam when $\varphi_{max} = 45^{\circ}$.

approach proposed in the present study, since the structure in Figure 19(b-2) is fully printable with the identified multi-axis build directions, the compliance increase is zero.

4.4. Cantilever beam example

To examine the influence of different grid size for the regular gird approach, a cantilever beam example is investigated in this section. The case description is presented in Figure 22 (a), where the design domain has a length (L) of 160 mm and a height (H) of 80 mm; the magnitude of the load (F) is 1.0 N and the load (R) is 0.5 N, the volume fraction (f) is 0.4. The solution obtained using the traditional topology optimisation is depicted in Figure 22(b).

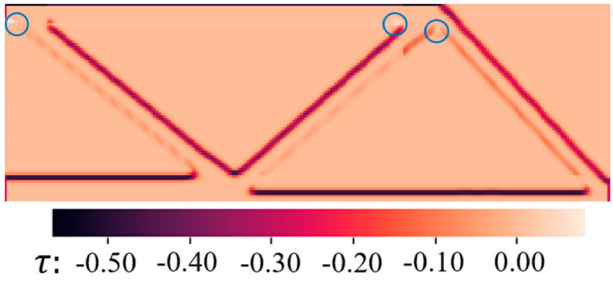


Figure 21. Elemental overhang violation value τ for the structure in Figure 19(a-2), with the unprintable elements marked with blue circles.

During the printing plan optimisation step, a value of $\varphi_{max} = 45^{\circ}$ is used, while three different zone arrangements, shown in Figure 23(a-1), (a-2) and (a-3), are considered. When 3-axis AM is employed, the printable ratio of Figure 22(b) is 23.63%. In the first step, where the structure is kept unchanged and the local build directions from the printing plane optimisation are utilised, the associated r_{unp} values are reduced to 11.7%, 9.29%, 6.29% for the zone arrangements in Figure 23 (a-1), (a-2) and (a-3), respectively. Subsequently, after the structural re-optimisation, the r_{unp} values are further reduced to near 0. The compliance sacrifice values (i.e. relative to Figure 22(b)) are 6.65% 1.88% and 0.94% for Figure 23 (b-1), (b-2) and (b-3), respectively. The results display a reduction in structural compliance as the decrease in grid size. This is because smaller grid sizes lead to increased freedom for the printing surfaces, which further reduces the structural sacrifice caused by the overhang constraint. A convergence history for the re-optimisation of Figure 23(2) is shown in Figure 24. It is worth noting that r_{unp} remains low (i.e. $\leq 0.1\%$) throughout the convergence process.

4.5. Influence of printing surface turning angles

As shown in Figure 3, multi-axis AM is associated with collision problems when a concave printing surface with a large turning angle φ_t is used. To address this

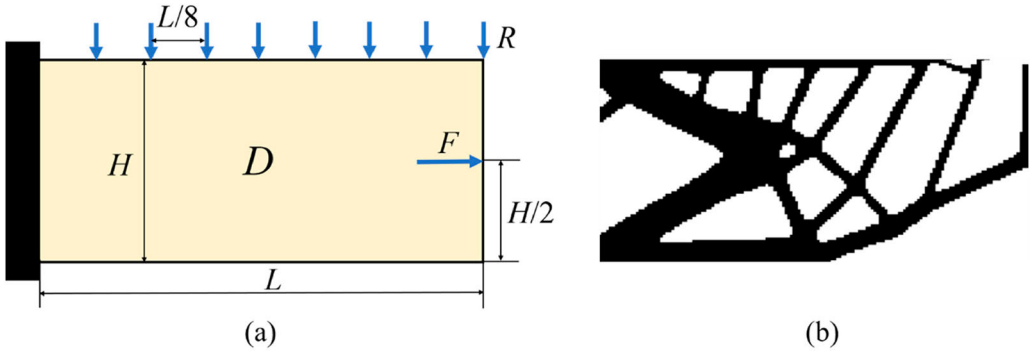


Figure 22. Cantilever beam example when volume fraction is 0.4; (a) design domain, load and support conditions; (b) solution obtained using traditional topology optimisation; the structural compliance $C = 326.10$ N mm.

problem, the constraint expressed by Equation (17d) is used to restrict the turning angles of the printing surfaces. Since the maximum turning angle $\varphi_{t,\,max}$ varies depending on the AM equipment and configuration (e.g. the proportion of the printing nozzle), the influence of $\varphi_{t,\,max}$ on the optimised solution is investigated in this section through the example of a simply-supported bridge. The case description is shown in Figure 25(a), with the design domain having a length L of 200 mm and a height H of 200 mm. The magnitude of the applied force F is 1.0 N and the allowable volume fraction f is taken as 0.1. The optimised solution from the traditional SIMP method is shown in Figure 25(b).

The zone arrangement for the printing plan optimisation is shown in Figure 25(b), with φ_{max} taken as 45°. Three different values of $\varphi_{t,\,max}$ were considered (i.e. $\varphi_{t,\,max} = 30^\circ,\ 45^\circ,\ 60^\circ$), with the unprintable ratio r_{unp} for all three optimised results being 4.54%. The r_{unp}

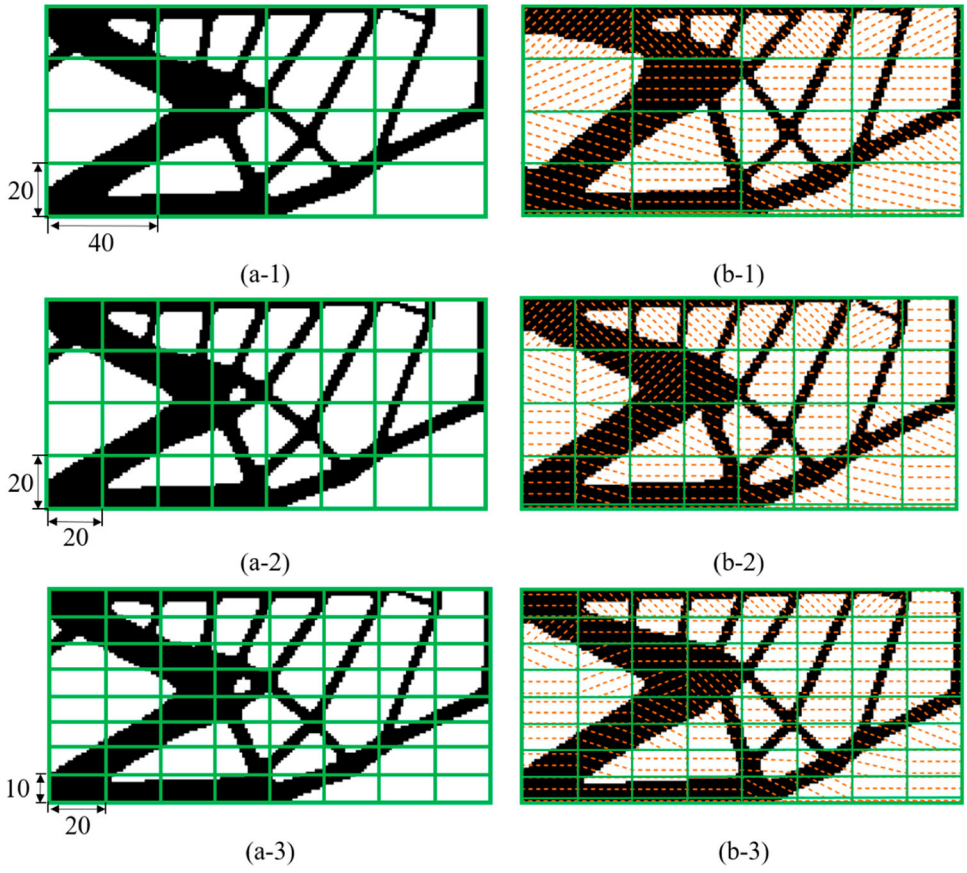


Figure 23. Optimised results for the cantilever example: (a) three zone arrangements with different grid size; (b) optimised solutions obtained using zone arrangements in (a), where the compliance in (1) $C = 347.79$ N mm; (2) $C = 332.26$ N mm; (3) $C = 329.17$ N mm.

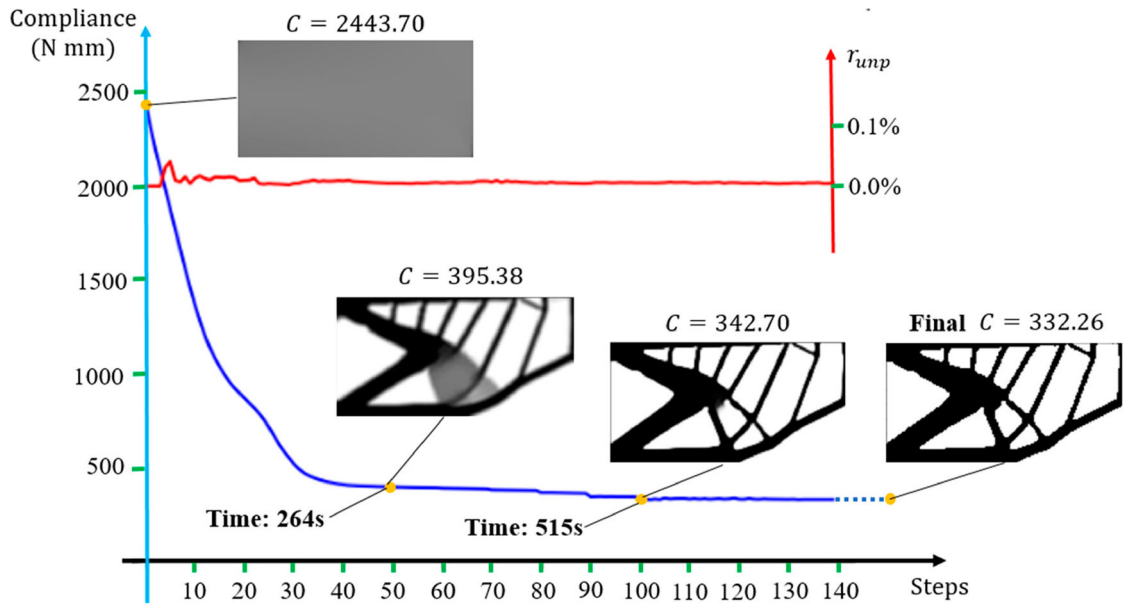


Figure 24. Convergence history and computational time of the re-optimisation step for cantilever beam under zone arrangement in Figure 23 (2).

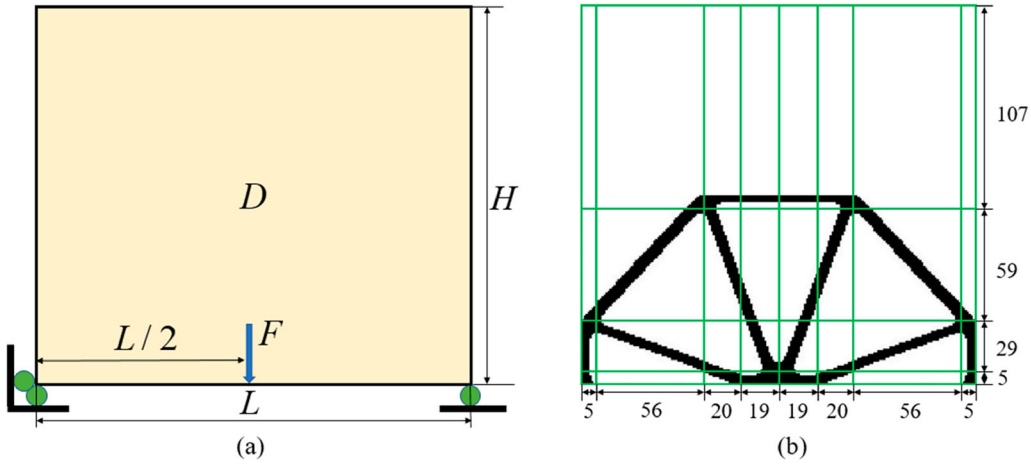


Figure 25. (a) Description of bridge example; (b) solution obtained with traditional topology optimisation, with dimensions in mm (structural compliance $C = 43.43$ N mm) and zone arrangements obtained from multi-axis AM optimisation.

values are relatively large due to the bottom boundary of the top horizontal member not being supported – see Figure 26. Therefore, to reduce r_{unp}, the re-optimisation approach is utilised, leading to the results shown in Figure 27. After completion of the re-optimisation, the r_{unp} values are reduced to nearly 0.00% for $\phi_{t,\,max} = 30^\circ$, 45°, 60°, respectively. Compared to Figure 25 (b), despite the marked changes in geometry of the structures shown in Figure 26 needed to address the overhang problem, the resulting compliance increase values are mild (less than 6.0%).

Since the top horizontal member is the most challenging part to print, it has essentially been modified to a three-member structure, as shown in Figure 27 (a-c). Consequently, the total structural height H is slightly increased

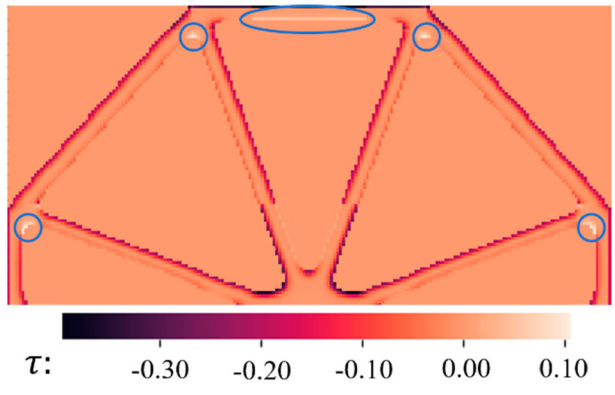


Figure 26. Elemental overhang violation value t obtained with the zone arrangement in Figure 25 (b) with $\varphi_{max} = 45^\circ$ and maximum turning angle $\varphi_{t,\,max} = 30^\circ, 45^\circ, 60^\circ$, with the unprintable elements highlighted within blue lines.

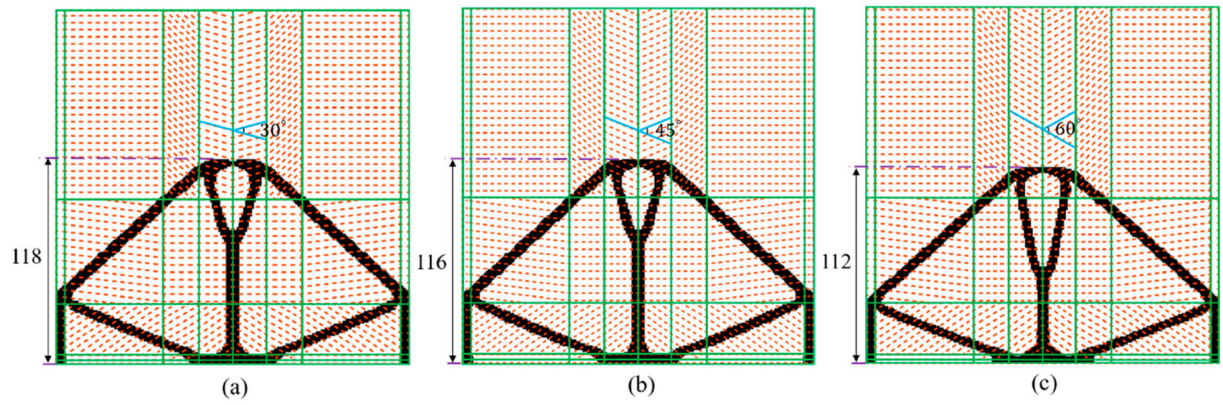


Figure 27. Optimised solutions of bridge example, with dimensions in mm: (a) solution obtained with $\phi_{t,\,max} = 30^\circ$ and $\varphi_{max} = 45^\circ$, $C = 46.04$ N mm; (b) solution obtained with $\phi_{t,\,max} = 45^\circ$ and $\varphi_{max} = 45^\circ$, $C = 45.26$ N mm (c) solution obtained with $\phi_{t,\,max} = 60^\circ$ and $\varphi_{max} = 45^\circ$, $C = 45.05$ N mm.

(from 100 mm in Figure 25 (b) to 118 mm in Figure 27 (a), 116 mm in Figure 27 (b) and 112 mm in Figure 27 (c)), suggesting that the overhang effect can be reduced by expanding the space of the design domain. Furthermore, it can be observed that concave printing surfaces are used in the zones associated with the top three-member structure, with their turning angles restricted by $\varphi_{t,\,max}$. When $\varphi_{t,\,max}$ is increased from 30° to 60° in Figure 27 (a-c), the concavity of the printing surface increases, leading to reductions in both the structural height and structural compliance. This finding is consistent with reality since large $\varphi_{t,\,max}$ values are associated with AM with sharp printing nozzles (i.e. high printing flexibility) and hence a reduced possibility of collisions. Therefore, the corresponding compliance sacrifice associated with the overhang constraints is reduced when $\varphi_{t,\,max}$ increases. The convergence history of re-optimisation when $\varphi_{t,\,max} = 30^\circ$ and $\varphi_{t,\,max} = 45^\circ$ is shown in Figure 28. In this example, r_{unp} remains at 0 throughout the convergence process.

5. Discussion

The numerical examples demonstrate the effectiveness of our proposed approach, which incorporates the overhang constraint associated with multi-axis AM. While smoothly curved printing surfaces are utilised in many other multi-axis AM studies [10], we assume the printing

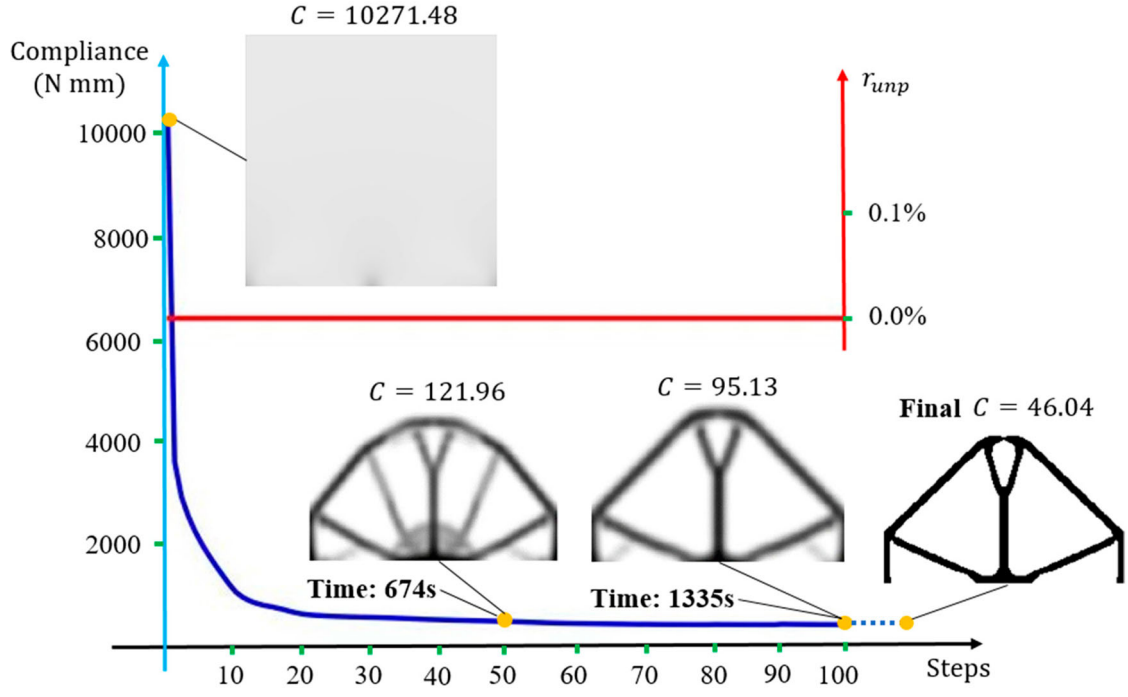


Figure 28. Convergence history of the re-optimisation step for the bridge example in Figure 27(a).

surfaces to be piecewise segments by restricting the each zone's local build direction to be constant. Although this treatment restricts the flexibility of the multi-axis AM, it greatly reduces the computational complexity and makes the printing plan optimisation problem linear (i.e. Equation (17)). In addition, we show that the restriction on printing flexibility is minor since the sacrifice in compliance is reduced to a negligible level (e.g. less than 6.0%). Therefore, the benefits of restricting the local build directions appear to outweigh the drawbacks.

As the first study on this approach, we solely focus on 2D problems. Nevertheless, the two-step approach can be adapted and expanded to address 3D scenarios, with key elements adjusted to suit the intricacies of these problems. For example, as shown in Figure 4, in 2D problems we use the one angle φ to represent the local build direction. When extended to 3D problems with O-XYZ axis (e.g. O as the origin point), the local build direction in 3D space can be effectively represented using two angle parameters. These two parameters indicate the angles of the projected vector on the XOZ plane and the YOZ plane, respectively. In addition, for the domain subdivision, whilst the regular grid approach can be directly used in 3D, the corner-detection technique that utilised in the joint-split approach (Section 3.1.1) could be substituted with a skeleton-extraction approach [46,47]. Moreover, during the re-optimisation step, the overhang constraint can be seamlessly extended to 3D following the guidelines provided in [26]. Considering the increase in structural complexity in 3D problem, the printing plan optimisation approach can be replaced by a more flexible curved printing surfaces [10] or space–time field-based approach [48].

It is also worth noting that the utilisation of the 'joint-split' approach can result in sudden changes in the local build directions at the joint positions, potentially affecting the mechanical performance of the structural joints. This issue can be mitigated by customising the printing tool paths to allow for smooth, curved transitions in the local build directions at the joint positions, which can be a potential topic for future research.

6. Conclusions

This study proposes a two-step topology optimisation approach for self-supporting structures considering overhang constraints for multi-axis AM (i.e. machines with rotatable base platforms). Different from previous studies based on 3-axis AM, in this approach both the structure and the corresponding printing plan (i.e. the shape of the printing surfaces) are optimised. In the first step, an optimised structure obtained from the traditional topology optimisation serves as the starting point for a printing plan optimisation problem. This problem is solved to identify the printing surfaces that can achieve the maximum printable proportion of a given structure. Since multi-axis AM allows for different build directions to be used during the printing process, in the printing plan optimisation, the design domain is subdivided into a number of zones, with each zone having a specific build direction. Nevertheless, since the structure is kept unchanged in this first step, the identified multi-axis printing plan cannot guarantee that the obtained printable proportion is satisfactory. Therefore, in the second step, a novel re-optimisation approach is proposed to further alleviate the overhang problem by modifying the structure according to the printing surfaces identified in the first step.

Four numerical examples have been presented to demonstrate the effectiveness of the proposed approach, and the following conclusions can be drawn:

- Compared to the 3-axis-based approaches, the proposed multi-axis-based approach can significantly reduce (if not eliminate) the compliance sacrifice caused by the overhang constraint. In the two-bar example, the previous 140.3% compliance sacrifice in 3-axis AM is reduced to 2.1% by adopting the multi-axis AM. In the MBB beam example, the compliance sacrifice is reduced from 20.6% to 0.
- For the domain subdivision, the regular grid approach is more inclined to yield satisfactory results in problems with high volume fractions (e.g. ≥ 0.5) as these problems are less susceptible to the overhang effect. Conversely, in situations with low volume fractions, the truss-like nature of the optimised structure can be leveraged. By first detecting the structure joints and then positioning the zone split lines at the joint locations, satisfactory solutions can also be achieved.
- Unlike 3-axis AM, collisions can occur in multi-axis AM when concave surfaces are printed. To reduce the possibility of potential collisions, an angle constraint is used to restrict the maximum turning angle $\varphi_{t,\,max}$ of the optimised printing surface (i.e. restricting the maximum printing surface concavity). The results show that small values of $\phi_{t,\,max}$ result in increases in structural compliance. Nevertheless, due to the high flexibility of multi-axis AM (i.e. allowing multiple build directions), in the examined examples, the obtained compliance sacrifices, which were brought about by the overhang constraints, are all mild (i.e. less than 7.0%).

Disclosure statement

No potential conflict of interest was reported by the author(s).

Funding

This work was supported by the National Natural Science Foundation of China [Grant Number: 52208215], the Natural Science Foundation of Zhejiang Province [Grant Number: LQ22E080008], the Centre for Balance Architecture of Zhejiang University and the Australian Research Council [Grant Number: FL190100014].

References

[1] Andreassen E, Clausen A, Schevenels M, et al. Efficient topology optimization in MATLAB using 88 lines of code. Struct Multidiscip Optim. 2011;43(1):1–16. doi: 10.1007/s00158-010-0594-7

[2] Bendsøe M, Kikuchi N. Generating optimal topologies in structural design using a homogenization method. Comput Methods Appl Mech Eng. 1988;71(2):197–224. doi: 10.1016/0045-7825(88)90086-2

[3] Bendsøe MP, Sigmund O. *Topology optimization: "theory, methods, and applications"*. Springer; 2011. https://link.springer.com/book/10.1007978-3-662-05086-6

[4] Sigmund O. A 99 line topology optimization code written in Matlab. Struct Multidiscip Optim. 2001;21(2):120–127. doi: 10.1007/s001580050176

[5] Zadpoor AA. Design for additive bio-manufacturing: from patient-specific medical devices to rationally designed meta-biomaterials. Int J Mol Sci. 2017;18(8):1607. doi: 10.3390/ijms18081607

[6] Zhang Y, Shan Y, Liu X, et al. An integrated multi-objective topology optimization method for automobile wheels made of lightweight materials. Struct Multidiscip Optim. 2021;64(3):1585–1605. doi: 10.1007/s00158-021-02913-3

[7] Zhu J-H, Zhang W-H, Xia L. Topology optimization in aircraft and aerospace structures design. Arch Comput Methods Eng. 2016;23(4):595–622. doi: 10.1007/s11831-015-9151-2

[8] Gardner L. Metal additive manufacturing in structural engineering – review, advances, opportunities and outlook. Structures. 2023;47:2178–2193. doi: 10.1016/j.istruc.2022.12.039

[9] Ye J, Kyvelou P, Gilardi F, et al. An end-to-end framework for the additive manufacture of optimized tubular structures. IEEE Access. 2021;9:165476–165489. doi: 10.1109/ACCESS.2021.3132797

[10] Zhang T, Fang G, Huang Y, et al. S3-slicer: a general slicing framework for multi-axis 3D printing. J ACM Trans Graph. 2022;41(6):1–15. doi: 10.1145/3550454.3555516

[11] Delissen A, Boots E, Laro D, et al. Realization and assessment of metal additive manufacturing and topology optimization for high-precision motion systems. Addit Manufact. 2022;58:103012. doi: 10.1016/j.addma.2022.103012

[12] Liu Q, Xu R, Zhou Y, et al. Metamaterials mapped lightweight structures by principal stress lines and topology optimization: methodology, additive manufacturing, ductile failure and tests. Mater Des. 2021;212:110192. doi: 10.1016/j.matdes.2021.110192

[13] Bi M, Tran P, Xia L, et al. Topology optimization for 3D concrete printing with various manufacturing constraints. Addit Manufact. 2022;57:102982. doi: 10.1016/j.addma.2022.102982

[14] Gao W, Zhang Y, Ramanujan D, et al. The status, challenges, and future of additive manufacturing in engineering. Comput Aided Des. 2015;69:65–89. doi: 10.1016/j.cad.2015.04.001

[15] Guest JK, Zhu M. *Casting and milling restrictions in topology optimization via projection-based algorithms, Design Automation Conference*. New York (NY); 2012. p. 913–920. doi: 10.1115/DETC2012-71507

[16] Mu Z, Yang Y, Gaynor AT, et al. *Considering constructability in structural topology optimization, structures congress*. Boston (MA); 2014. p. 2754–2764. doi: 10.1061/9780784413357.241

[17] Wang D, Yang Y, Yi Z, et al. Research on the fabricating quality optimization of the overhanging surface in SLM process. Int J Adv Manuf Technol. 2013;65(9):1471–1484. doi: 10.1007/s00170-012-4271-4

[18] Strano G, Hao L, Everson RM, et al. A new approach to the design and optimisation of support structures in additive manufacturing. Int J Adv Manuf Technol. 2013;66(9):1247–1254. doi: 10.1007/s00170-012-4403-x

[19] van de Ven E, Ayas C, Langelaar M, et al. Accessibility of support structures in topology optimization for additive manufacturing. Int J Numer Meth Eng. 2021;122(8):2038–2056. doi: 10.1002/nme.6611

[20] Leary M, Merli L, Torti F, et al. Optimal topology for additive manufacture: a method for enabling additive manufacture of support-free optimal structures. Mater Des. 2014;63:678–690. doi: 10.1016/j.matdes.2014.06.015

[21] Li Z, Zhang DZ, Dong P, et al. A lightweight and support-free design method for selective laser melting. Int J Adv Manuf Technol. 2017;90(9):2943–2953. doi: 10.1007/s00170-016-9509-0

[22] Gaynor AT, Guest JK. Topology optimization considering overhang constraints: eliminating sacrificial support material in additive manufacturing through design. Struct Multidiscip Optim. 2016;54(5):1157–1172. doi: 10.1007/s00158-016-1551-x

[23] Langelaar M. An additive manufacturing filter for topology optimization of print-ready designs. Struct Multidiscip Optim. 2017;55(3):871–883. doi: 10.1007/s00158-016-1522-2

[24] Langelaar M. Combined optimization of part topology, support structure layout and build orientation for additive manufacturing. Struct Multidiscip Optim. 2018;57(5):1985–2004. doi: 10.1007/s00158-017-1877-z

[25] Pellens J, Lombaert G, Lazarov B, et al. Combined length scale and overhang angle control in minimum compliance topology optimization for additive manufacturing. Struct Multidiscip Optim. 2019;59(6):2005–2022. doi: 10.1007/s00158-018-2168-z

[26] Zhang K, Cheng G, Xu L. Topology optimization considering overhang constraint in additive manufacturing. Comput Struct. 2019;212:86–100. doi: 10.1016/j.compstruc.2018.10.011

[27] Garaigordobil A, Ansola R, Santamaría J, et al. A new overhang constraint for topology optimization of self-

supporting structures in additive manufacturing. Struct Multidiscip Optim. 2018;58(5):2003–2017. doi: 10.1007/s00158-018-2010-7

[28] Allaire G, Dapogny C, Estevez R, et al. Structural optimization under overhang constraints imposed by additive manufacturing technologies. J Comput Phys. 2017;351:295–328. doi: 10.1016/j.jcp.2017.09.041

[29] Wei G, Zhang Y, Nazzetta DC, et al. *Revomaker: enabling multi-directional and functionally-embedded 3d printing using a rotational cuboidal platform. Proceedings of the 28th annual ACM Symposium on User Interface Software & Technology*. Charlotte (NC); 2015. p. 437–446. doi: 10.1145/2807442.2807476

[30] Gibson BT, Mhatre P, Borish MC, et al. Controls and process planning strategies for 5-axis laser directed energy deposition of Ti-6Al-4V using an 8-axis industrial robot and rotary motion. Addit Manufact. 2022;58:103048. doi: 10.1016/j.addma.2022.103048

[31] Wulle F, Gorke O, Schmidt S, et al. Multi-axis 3D printing of gelatin methacryloyl hydrogels on a non-planar surface obtained from magnetic resonance imaging. Addit Manufact. 2022;50:102566. doi: 10.1016/j.addma.2021.102566

[32] Gao Y, Wu L, Yan DM, et al. Near support-free multi-directional 3d printing via global-optimal decomposition. Graph Models. 2019;104:101034. doi: 10.1016/J.GMOD.2019.101034

[33] Karasik E, Fattal R, Werman M. Object partitioning for support-free 3D-printing. Comput Graph Forum. 2019;38. doi: 10.1111/cgf.13639

[34] Wu C, Dai C, Fang G, et al. General support-effective decomposition for multi-directional 3-D printing. IEEE Trans Autom Sci Eng. 2020;17(2):599–610. doi: 10.1109/TASE.2019.2938219

[35] Dai C, Wang C, Wu C, et al. Support-free volume printing by multi-axis motion. ACM Trans Graph. 2018;37(4):1–14. doi: 10.1145/3197517.3201342

[36] Xie F, Jing X, Zhang C, et al. Volume decomposition for multi-axis support-free and gouging-free printing based on ellipsoidal slicing. Comput Aided Des. 2022;143:103135. doi: 10.1016/j.cad.2021.103135

[37] Xu K, Li Y, Chen L, et al. Curved layer based process planning for multi-axis volume printing of freeform parts. Comput Aided Des. 2019;114:51–63. doi: 10.1016/j.cad.2019.05.007

[38] Li Y, He D, Wang X, et al. Geodesic distance field-based curved layer volume decomposition for multi-axis support-free printing; 2020. ArXiv abs/2003.05938.

[39] Bendsøe MP. Optimal shape design as a material distribution problem. Struct Optim. 1989;1(4):193–202. doi: 10.1007/BF01650949

[40] Zhou M, Rozvany GIN. The COC algorithm, part II: topological, geometrical and generalized shape optimization. Comput Methods Appl Mech Eng. 1991;89(1):309–336. doi: 10.1016/0045-7825(91)90046-9

[41] Bendsøe MP, Sigmund O. Material interpolation schemes in topology optimization. Arch Appl Mech. 1999;69(9):635–654. doi: 10.1007/s004190050248

[42] Xu S, Cai Y, Cheng G. Volume preserving nonlinear density filter based on Heaviside functions. Struct Multidiscip Optim. 2010;41(4):495–505. doi: 10.1007/s00158-009-0452-7

[43] Sigmund O, Petersson J. Numerical instabilities in topology optimization: a survey on procedures dealing with checkerboards, mesh-dependencies and local minima. Struct Multidiscip Optim. 1998;16(1):68–75. doi: 10.1007/BF01214002

[44] Harris CG, Stephens MJ. *A combined corner and edge detector. Alvey Vision Conference*. Manchester; 1988. p. 23.1–23.6. doi: 10.5244/C.2.23

[45] MOSEK optimizer API for python. Version 10.0.8. Available from: https://docs.mosek.com/latest/pythonapi/index.html

[46] Jootoo A, Lattanzi D. Extraction of structural system designs from topologies via morphological analysis and artificial intelligence; 2018.

[47] Wu C, Dai C, Fang G, et al. Automation, RoboFDM: a robotic system for support-free fabrication using FDM. IEEE Int Conf Robot Autom. 2017:1175–1180. doi: 10.1109/ICRA.2017.7989140

[48] Wang W, Munro D, Wang CCL, et al. Space-time topology optimization for additive manufacturing. Struct Multidiscip Optim. 2020;61(1):1–18. doi: 10.1007/s00158-019-02420-6